SHAPE MEMORY ALLOYS AS PHASE CHANGE MATERIALS FOR THERMAL ENERGY STORAGE

A Thesis

by

NATHAN HITE

Submitted to the Graduate and Professional School of
Texas A&M University
in partial fulfillment of the requirements for the degree of

MASTER OF SCIENCE

Chair of Committee,	Ibrahim Karaman
Committee Members,	Alaa Elwany
	Raymundo Arróyave
Head of Department,	Bryan Rasmussen

December 2021

Major Subject: Mechanical Engineering

ABSTRACT

Shape memory alloys (SMAs) have recently been demonstrated as effective phase change materials for thermal energy storage owing to their ability to undergo thermally driven reversible martensitic transformations. NiTi SMAs show excellent performance in high heat flux and transient thermal energy storage as quantified by Lu's figure of merit (FOM is equal to the product of density, thermal conductivity, and latent heat of transformation). However, NiTi SMAs are limited to transformation temperatures below 100°C, overall transformation ranges (OTR is equal to the difference between austenite finish (A_f) and martensite finish (M_f) temperatures) above 50°C, and thermal conductivity under 18 W/m·K. In the current work, the transformation characteristics and thermophysical properties of NiTiHf, NiTiCu, and CuZnAl SMAs were measured and analyzed to determine their thermal energy storage performance, aiming to overcome the limitations of NiTi. Alloys of varying composition within the NiTiHf, NiTiCu, and CuZnAl systems were fabricated, and their transformation temperatures, transformation enthalpies, densities, and thermal conductivities were measured. NiTiHf SMAs showed more than double the FOM value (3217 10^6 $J^2K^{-1}s^{-1}m^{-4}$) of NiTi (1478 10^6 $J^2K^{-1}s^{-1}m^{-4}$) with transformation temperatures ranging from 0 to beyond 500°C. The transformation enthalpies of the alloys were found to be strongly correlated with composition, having a significant effect on FOM values. NiTiCu SMAs showed A_f temperatures between -10 and 90 °C with FOM values up to 1048 10^6 $J^2K^{-1}s^{-1}m^{-4}$ and OTRs as low as 12°C. These properties make NiTiCu alloys excellent candidates for thermal energy storage

applications requiring frequent cycling or narrow operation temperature ranges. The thermophysical properties of the NiTiCu alloys were strongly dependent on composition, and alloys near 50 at. % Ti showed the highest FOM values. CuZnAl SMAs achieved the highest FOM values (up to 3463 10^6 $J^2K^{-1}s^{-1}m^{-4}$) due to their high thermal conductivities, which ranged from 59 to 75 W/m·K. CuZnAl alloys also showed overall transformation ranges as low as 12°C. The NiTiHf, NiTiCu, and CuZnAl alloy systems showed excellent thermal energy storage performance, greatly improving upon the capabilities of NiTi shape memory alloys and traditional phase change materials.

ACKNOWLEDGEMENTS

I would like to thank my committee chair, Dr. Ibrahim Karaman, and my committee members, Dr. Alaa Elway and Dr. Raymundo Arróyave, as well as my research collaborators, Darin Sharar, Adam Wilson, and Asher Leff, for their guidance and support throughout the course of this research.

Thanks also goes to my fellow researcher, Willie Trehern, for his hard work and companionship throughout our collaboration.

Finally, thanks to my mother, father, and brothers for their encouragement, love, and support throughout my graduate studies.

CONTRIBUTORS AND FUNDING SOURCES

Contributors

This work was supervised Professor Ibrahim Karaman of the Department of Mechanical Engineering, Professor Alaa Elwany of the Department of Industrial and Systems Engineering, and Professor Raymundo Arróyave of the Department of Materials Science and Engineering.

The arc-melted alloys studied in Chapter 2 were synthesized by Tejas Umale of the Department of Materials Science and Engineering. The experiments and analyses in Chapters 3 and 4 were conducted in part by William Trehern of the Department of Materials Science and Engineering. The thermal diffusivity data in all chapters was collected by Darin Sharar and Adam Wilson of the U.S. Army Research Laboratory.

All other work conducted for the thesis was completed by the student independently.

Funding Sources

Graduate study and research were supported by funding from U.S. Army Research Laboratory.

NOMENCLATURE

Acronyms

ASTM	American Society for Testing and Materials
DCFL	Direct Coupled Field-Effect Transistor Logic
DSC	Differential Scanning Calorimetry
DXF	Discovery Xenon Flash
EDM	Electrical Discharge Machining
EDS/EDX	Energy Dispersive X-Ray Spectroscopy
FET	Field-Effect Transistor
FOM	Figure of Merit
HEMT	High Electron Mobility Transistor
ICP-AES	Inductively Coupled Plasma Atomic Emission Spectroscopy
OTR	Overall Transformation Range
PCM	Phase Change Material
SMA	Shape Memory Alloy
SEM	Scanning Electron Microscopy
TES	Thermal Energy Storage
TGA	Thermogravimetric Analysis
VED	Volumetric Energy Density
XRD	X-Ray Diffraction

Variables

A_f	Austenite Finish Temperature
A_s	Austenite Start Temperature
c_p	Specific Heat Capacity
k	Thermal Conductivity
L	Latent heat of Transformation
M_f	Martensite Finish Temperature
M_s	Martensite Start Temperature
w_a	Weight in Air
w_s	Weight Submerged in Water
α	Thermal Diffusivity
ΔH_{AM}	Austenite to Martensite Transformation Enthalpy
ΔH_{MA}	Martensite to Austenite Transformation Enthalpy
ρ	Density
ρ_w	Density of Water

TABLE OF CONTENTS

Page

LIST OF FIGURES

LIST OF TABLES

Page

1. INTRODUCTION

Phase change materials (PCMs) are widely used in thermal energy storage and management applications due to their ability to absorb and release large amounts of thermal energy upon phase transformation while maintaining nearly constant temperature. Traditional PCMs such as paraffin, polymers, and salt hydrates have been implemented in a variety of applications including building temperature regulation, battery thermal management, and solar air and water heating [1]. For such applications, PCM performance can be quantified by volumetric energy density (VED), given by $VED = \rho \cdot L$, where ρ is density and L is latent heat of transformation. This performance metric, which quantifies the amount of thermal energy which can be stored within a given volume of a PCM, is useful in many cases, however it does not account for the rate at which the thermal energy must be stored and released. In thermal management applications where fast transient or high-power thermal transport is required, such as in microelectronic thermal management, VED is an insufficient metric to describe the performance of a given PCM. Recognizing this, Lu developed a PCM figure of merit (FOM) which accounts for transient thermal transport effects, and is given by $FOM = \rho \cdot L \cdot k$, where ρ is density, L is latent heat of transformation, and k is thermal conductivity [2].

Unfortunately, traditional PCMs show low FOM values, typically ranging between 20 and 400 $10^6 \cdot J^2/K \cdot s \cdot m^4$ [3], making them unsuitable for many high-power thermal energy storage and management applications. Implementation of traditional PCMs is further hindered by their solid-liquid phase transformation, which requires fluid

containment structures to prevent leakage of the liquid phase. However, recent work has shown that the ability of shape memory alloys (SMAs) to undergo forward and reverse martensitic transformation (exothermic and endothermic transformations, respectively) allows them to function similarly to traditional PCMs, absorbing and releasing large amounts of thermal energy while maintaining nearly constant temperature. Sharar et al. showed NiTi SMAs to be excellent high-FOM PCM candidates, exhibiting FOM values as high as 1478 $10^6 \cdot J^2/K \cdot s \cdot m^4$, and demonstrating the ability to reduce the maximum temperatures experienced by a system undergoing joule heating [4]. The high FOM value observed in NiTi is attributed to its high density (6239 kg/m^3) and high thermal conductivity (17.6 $W/m \cdot K$) in comparison to traditional PCMs such as paraffin, which has low density (790 kg/m^3) and low thermal conductivity (0.167 $W/m \cdot K$) [3]. The solid-solid transformations undergone by SMAs give them another advantage over traditional PCMs by eliminating the need for fluid containment and simplifying implementation.

Despite the promising performance and advantages offered by NiTi SMAs over traditional PCMs, NiTi suffers from its own set of limitations. First, NiTi transformation temperatures are generally limited to 100°C and below, excluding NiTi from high temperature thermal energy storage and management applications. For example, SiC electronics, high electron mobility transistor (HEMT) direct-coupled field-effect transistor (FET) logic (DCFL) integrated circuits, and microwave semiconductor devices have maximum operation temperature ranges of 150°C, 375°C, and 700°C respectively [5-7], requiring PCM thermal management solutions with high-temperature operation capabilities. In addition to operation temperature limitations, NiTi SMAs are limited by

their large overall transformation ranges (OTR is defined as austenite finish temperature minus martensite finish temperature (A_f-M_f)) which often exceed 50°C. This excludes NiTi SMAs from use in thermal management applications requiring narrow operation temperature ranges such as solid-state lasers which may be limited to operation temperature windows as narrow as 10°C [8]. Narrow overall transformation range in PCMs is also desirable because it allows for increased thermal cycling frequency and therefore provides more effective thermal management. Finally, despite the large improvement in FOM of NiTi SMAs over traditional PCMs, alternative SMA systems may be capable of achieving even higher FOM values and greater PCM performance.

The vast potential of SMAs in thermal energy storage and management applications, coupled with the limitations shown in NiTi SMAs, provides great motivation to evaluate alternative SMA systems for their potentially superior PCM performance. Currently, the PCM performances of alternative SMA systems are largely unknown as they have not been directly studied and reported in literature, and the relevant thermophysical material properties are scarcely reported. The current work investigates the transformation characteristics and thermophysical properties of alternative SMA systems in order to evaluate their potential PCM performance. Due to their ability to achieve high transformation temperatures, NiTiHf SMAs are explored as potential PCMs for high-temperature thermal energy storage. NiTiCu SMAs, which have been shown to achieve overall transformation ranges much lower than those of NiTi, are investigated for use in thermal energy storage applications which require frequent thermal cycling or

narrow operation temperature ranges. Finally, CuZnAl SMAs are studied as potential high-thermal conductivity, high-FOM PCMs for thermal energy storage.

2. NITIHF SHAPE MEMORY ALLOYS AS PHASE CHANGE THERMAL STORAGE MATERIALS[1]

2.1. Introduction

Thermal energy storage (TES) using shape memory alloys (SMAs) offers new design, integration, and performance opportunities in a wide range of technologies. This is particularly true for emerging electronic and photonic media [9, 10] that require high-power and fast-transient thermal energy storage [4], not possible with traditional organic and salt hydrate phase change materials (PCMs) [11]. Binary nickel titanium (NiTi) SMAs have been demonstrated for this purpose, with great effect, due to their high volumetric latent heat, approaching or often exceeding that of standard organic PCMs (225 MJ/m^3 [3]), high thermal conductivity, approaching 28 $Wm^{-1}K^{-1}$ [12], excellent corrosion resistance [13-15], high strength and ductility [16-21], and good formability via traditional thermomechanical processing [16, 20-23]. In contrast to solid-liquid phase transformations, which by definition melt upon heating, solid-solid phase transformations remain mechanically solid and self-supporting, thus eliminating the need for encapsulation. Despite the vast potential, the narrow temperature range of operability, generally not exceeding 100°C, and large temperature hysteresis (defined as A_f-M_s, where M_s and A_f are martensite start and austenite finish transformation temperatures,

[1]Reprinted with permission from "NiTiHf shape memory alloys as phase change thermal storage materials" by N. Hite, D.J. Sharar, W. Trehern, T. Umale, K.C. Atli, A.A. Wilson, A.C. Leff, I. Karaman, 2021. *Acta Materialia*, 218, 117175, Copyright 2021 by Elsevier Ltd.

respectively), often exceeding 30°C, has disqualified NiTi SMAs from many specific technology spaces. For example, emerging laser diodes may require forward and reverse transformations in the span of 10°C or less [8] and SiC electronics routinely operate at temperatures exceeding 150°C, as is the case for electric vehicle-based devices [24]. AlGaN and GaN high electron mobility transistor (HEMT) direct-coupled field-effect transistor (FET) logic (DCFL) integrated circuits have been shown to operate at as high as 375°C [6], and emerging microwave semiconductor devices fabricated out of Si, GaAs, 4H-SiC, and GaN have maximum operation temperatures ranging from 300 to 700°C [7], requiring thermal energy storage solutions which function well above the 100°C limitation of NiTi.

Previous studies in the literature have demonstrated that transformation temperatures and functional properties of NiTi can be tailored by alloying with Hf, Pd, Pt, Au, and Zr for high temperature operations up to 500°C [25-37]. With these alloy systems, it is anticipated that SMAs could be utilized in a broader range of applications and designs than experimentally validated for NiTi alone. NiTiHf was selected for this study due to its high temperature operation capability. Moreover, with a relatively low thermal hysteresis in some compositions [38], NiTiHf demonstrates high density and transformation enthalpy, making it a candidate PCM with potentially high figure of merit (FOM). In the present study, the FOM used is the one derived by Lu [2], which solves the Neumann-Stefan problem for melting of a semi-infinite material. The general form is $FOM = k \cdot L \cdot \rho$, where k is the high temperature phase (austenite or liquid) thermal conductivity, L is the latent heat of transformation, and ρ is the density of the high temperature phase, as

described by Shamberger [39] and Shao et al. [40]. A high value of FOM is desirable for PCMs because it represents a material's ability to rapidly store and release large quantities of thermal energy in a small volume. $L \cdot \rho$ defines the volumetric energy storage capacity, while k determines the rate at which thermal energy can travel from the heat source, through the transformed material, i.e. austenite, to the phase front within the PCM. FOM applies to any material exhibiting endothermic phase transitions upon heating and has recently been used to demonstrate the superiority of SMAs for high power (or short time-response) thermal energy storage applications. While typically not explicitly reported, these material properties are important in standard use cases of materials exhibiting reversible martensitic transformations (such as shape memory actuation and elastocaloric cooling). Optimization for these uses requires careful consideration of thermal conductivity and heat capacity to control work input, cooling work, and thermal time constant. Therefore, FOM and constituent properties are good indicators of the behavior of materials exhibiting reversible martensitic transformations.

Beyond FOM, NiTiHf alloys exhibit clear trends in transformation temperatures with changing composition [38, 41], making them tunable to specific PCM applications through composition control. Umale et al. [38] mapped the martensite start (Ms) temperature and thermal hysteresis values of NiTiHf alloys for Ni contents between 49.8 at. % and 51.2 at. % and Hf contents between 0 at. % and 30 at.%. The results showed that the sensitivity of M_s temperature to changes in composition can be approximated as 360°C/at. % for Ni (calculated as the slope of the line connecting the M_s temperatures of $Ni_{50.3}Ti_{29.7}Hf_{20}$ and $Ni_{51}Ti_{29}Hf_{20}$) in $NiTiHf_{20}$ alloys and 15°C/at. % for Hf (calculated as

the slope of the line connecting the M_s temperatures of $Ni_{50.3}Ti_{44.7}Hf_5$ and $Ni_{50.3}Ti_{24.7}Hf_{25}$) in $Ni_{50.3}TiHf$ alloys, for example. Although the sensitivity of transformation temperatures to composition is not constant with respect to composition, the data can be interpolated to achieve NiTiHf compositions with any desired M_s temperature between 0 and 500°C. In the same study, thermal hysteresis was found to be strongly correlated with Hf content, increasing between 0 at. % and 10 at. % Hf, decreasing between 10 at. % and 20 at. % Hf, and increasing between 20 at. % and 30 at. % Hf.

In the present work, select NiTiHf compositions from the work of Umale et al. [38] are examined in order to determine their potential as high-temperature solid-solid PCMs. One of the goals of this study is to determine their thermophysical properties such as thermal conductivity, transformation enthalpy, density, and thermal hysteresis that are paramount in TES applications, but generally overlooked in previous studies on many SMAs, in particular, thermal conductivity. The present work is expected to advance the state of TES technology by extending the temperature range of SMA TES applications and demonstrating improved SMA PCM performance. Furthermore, the work herein is expected to provide a new impetus for the SMA community to pay closer attention to thermal transport properties of SMAs, which are mostly overlooked and not widely reported, despite the fact that they are quite critical in applications at the device and system level.

2.2. Experimental Procedures

2.2.1. Material synthesis and sample preparation

NiTiHf alloys with varying compositions were fabricated using arc-melting of pure elements under argon. The samples were flipped and re-melted six times followed by solution heat treatment under argon atmosphere at 1050°C for 2 h to ensure chemical homogeneity. All samples were quenched in water at room temperature immediately following the heat treatment. From each sample, 3 mm diameter and 1 mm thick discs were cut using wire electrical discharge machining (wire-EDM) for differential scanning calorimetry (DSC) analysis. Based on the measured transformation temperatures, thermal hysteresis, and transformation enthalpy of these samples, $Ni_{50.3}Ti_{29.7}Hf_{20}$ (at. %) was chosen and fabricated in larger dimensions for thermal diffusivity measurements (in the form of a cylindrical rod with 31.75 mm diameter). In order to best demonstrate the PCM performance of NiTiHf, the selection criteria for the composition of the bulk alloy included maximum transformation enthalpy with an austenite finish (A_f) temperature above 200°C and thermal hysteresis below 40°C. The bulk alloy was fabricated using vacuum induction skull melting followed by hot extrusion at 900°C (with a 6:1 area reduction) and solution heat treatment at 900°C for 1 h. From the bulk sample, 8 mm diameter and 1 to 2 mm thick discs were wire-EDM cut for laser flash thermal diffusivity analysis.

2.2.2. Density Measurements

Archimedes' method was used to measure the density of NiTiHf samples of varying composition. Samples were weighed both in air and while submerged in water of a known temperature. Using these two measurements, the density of each sample was calculated as $\rho = \rho_w * \frac{w_a}{w_a - w_s}$, where ρ is the density of the sample being measured, ρ_w is the density of water at the measured temperature, w_a is the weight of the sample in air, and w_s is the weight of the sample measured while submerged in water.

Measurement of transformation temperatures and thermophysical properties

The transformation temperatures and the enthalpy of transformation of all NiTiHf compositions, as well as the specific heat capacity of the bulk NiTiHf alloy as a function of temperature, were measured using a TA Instruments Q2000 differential scanning calorimeter. For transformation temperature and transformation enthalpy measurements, each sample underwent two heating/cooling cycles between -150°C and 400°C at a rate of 10°C/min. In accordance with the ASTM F2004 standard [42], martensite finish (M_f), M_s, austenite start (A_s) and A_f transformation temperatures were determined by the intercept method whereby tangent lines are drawn parallel to the baseline and transformation peak slopes. The temperature at which the transformation slope tangent and baseline tangent intersect is considered to be the transformation temperature. For compositions which transformed above 400°C, a TA Instruments SDT Q600 DSC/TGA machine was used to measure differential heat flow up to 700°C at a rate of 10°C/min in order to discern transformation temperatures. The thermal hysteresis of each sample was calculated as the difference between its A_f and M_s temperatures. Enthalpy

of transformation was determined by integrating the heat flow under the transformation peak with respect to time. Specific heat capacity was measured during a single heating cycle from -150 to 400°C with a heating rate of 10°C/min. The thermal diffusivity of the bulk NiTiHf samples was measured using a TA Instruments DXF 200 high-speed Xenon-pulse delivery source and solid-state PIN detector. Measurements were taken at approximately 50°C temperature intervals from -150 to 150°C, with smaller temperature intervals used within the transformation range of 150 to 215°C. Using a similar temperature interval scheme, the measurements were repeated during cooling from 215 to -150°C. Thermal conductivity, k was then calculated as $k = \alpha \cdot \rho \cdot c_p$, where α is thermal diffusivity, ρ is density, and c_p is specific heat capacity. Due to the limited temperature range of the TA Instruments DXF 200, the number of candidate alloys for thermal conductivity measurement in the austenite phase was limited. Because the thermal conductivity of the austenite phase is used in calculating the FOM, alloys with A_f temperatures above the upper temperature limit of the instrument could not be considered for thermal conductivity measurement.

2.3. Results and Discussion

From among the 33 previously studied NiTiHf alloys [38] with known transformation temperatures, 10 compositions were chosen for thermophysical property evaluation (Table 2.1). These compositions were selected to represent a wide range of Ni and Hf contents, transformation temperatures, transformation enthalpies, and thermal hysteresis values. The bulk alloy composition (nominally $Ni_{50.3}Ti_{29.7}Hf_{20}$) was

chosen based on the high transformation temperature, high transformation enthalpy, and low thermal hysteresis criteria as previously described.

Table 2.1. Fabrication method, composition, transformation temperatures [38], exothermic enthalpy of transformation, and thermal hysteresis for NiTiHf alloys of varying compositions. The compositions are nominal, based on the molar ratio of pure elements added to the melt. For the induction melted sample, the composition as measured by ICP-AES (inductively coupled plasma atomic emission spectroscopy) is listed in parentheses below the nominal composition. Transformation temperatures and transformation enthalpies are measured through DSC.

Fabrication	**Composition (at. %)**	**M_f (°C)**	**M_s (°C)**	**A_s (°C)**	**A_f (°C)**	**Enthalpy A-M (J/g)**	**Hysteresis (°C)**
Arc Melted	$Ni_{50.3}Ti_{34.7}Hf_{15}$	105	144	158	184	22.6	40
	$Ni_{50.3}Ti_{29.7}Hf_{20}$	238	258	274	289	32.5	31
	$Ni_{50.3}Ti_{24.7}Hf_{25}$	265	345	333	440	20.1	95
	$Ni_{50.3}Ti_{19.7}Hf_{30}$	413	487	583	622	12.2	135
	$Ni_{50.7}Ti_{34.3}Hf_{15}$	-18	26	41	76	7.2	50
	$Ni_{50.7}Ti_{29.3}Hf_{20}$	98	142	133	170	16.1	28
	$Ni_{50.7}Ti_{24.3}Hf_{25}$	214	263	274	334	16.3	71
	$Ni_{51}Ti_{29}Hf_{20}$	-13	3	36	52	6.6	49
	$Ni_{51}Ti_{24}Hf_{25}$	74	92	109	124	9.1	32
	$Ni_{51.2}Ti_{18.8}Hf_{30}$	106	140	136	162	14.4	22
Induction Melted	$Ni_{50.3}Ti_{29.7}Hf_{20}$ ($Ni_{50.8}Ti_{29.6}Hf_{19.4}$)	128	163	172	193	18.7	30

2.3.1. Density

The effect of compositional variation on the density of NiTiHf SMAs was considered. Since the variation in Ni content was low (less than 1 at. %) in the alloys studied (Table 2.1), measured density values did not differ significantly. However, the Hf content variation from 15 at. % to 30 at. % showed a measurable influence on the density of the alloys (Fig. 1). As expected, density shows a linearly increasing trend with increasing Hf content; this can be attributed to the high density of Hf (13.31 g/cm^3) in comparison to Ni and Ti (8.90 and 4.54 g/cm^3, respectively). The trend in density can be approximated by a linear regression model (black dashed line) given by: $\rho = 141 \cdot Hf + 6062$, where ρ is density in kg/m^3 and Hf is hafnium content in at.%. Inputting a Hf content of zero into the regression model yields a predicted density for binary NiTi of 6062 kg/m^3. This density prediction for binary NiTi agrees with measured literature values [4, 43] to within 3 - 6%, indicating that the fidelity of this regression model extends to lower Hf percentages than those studied here. Therefore, this model can be used as a tool to predict the density of the compositions from NiTi to $NiTiHf_{30}$ with reasonable accuracy. The density difference between the most and least dense NiTiHf alloys measured is 30%, suggesting that increasing Hf content should have a measurable impact on the FOM through density increase. However, the effects of varying thermal conductivity and enthalpy of transformation on the FOM of NiTiHf alloys must also be considered.

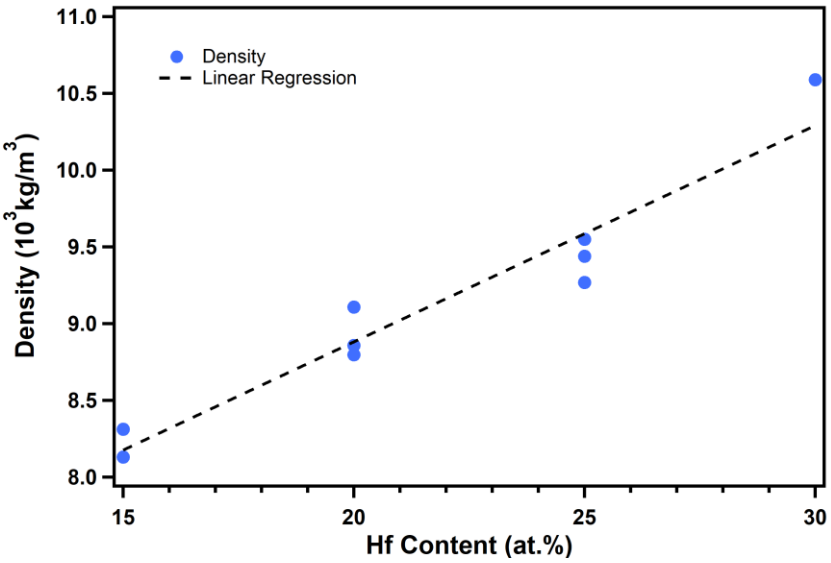

Fig. 2.1. Density of NiTiHf alloys (measured by Archimedes' method) as a function of Hf content. The dashed line represents a linear regression fit to the data, yielding a prediction equation given by: $\rho = 141 \cdot Hf + 6062$, where ρ is density in kg/m^3 and Hf is hafnium content in at. %.

2.3.2. Transformation Enthalpy and Thermal Hysteresis

The enthalpy of transformation values of the 11 studied samples are listed in Table 2.1. The measured NiTiHf transformation enthalpy values (endothermic) range from 6.6 to 32.5 J/g (corresponding to $Ni_{51}Ti_{29}Hf_{20}$ and $Ni_{50.3}Ti_{29.7}Hf_{20}$, respectively) and have an average value of 16.0 J/g. This wide range in transformation enthalpies, wherein the largest value is nearly 5 times the smallest value, indicates that transformation enthalpy variation in NiTiHf alloys has a much greater influence on the FOM value than density variation (the highest density value is only 1.3 times the lowest value). Because of this

significant influence of transformation enthalpy on the FOM, it is important to understand the relationship between chemical composition and transformation enthalpy so that high-FOM compositions can be targeted.

Fig. 2.2 illustrates the relationship between transformation enthalpy and composition in solution heat treated NiTiHf alloys with the thermal hysteresis of each alloy denoted by the color of its corresponding marker. For near equiatomic NiTi, it is well-known that increasing Ni content produces decreasing transformation enthalpy [25]. This decrease is attributed to the stabilization of B2 phase with increasing Ni antisite defects and the reduction of the monoclinic angle β, the latter bringing about an increased crystallographic compatibility between the transforming phases [25]. NiTiHf follows this trend for compositions with Hf content of 25 at. % or less as shown by the constant Ni content curves. This trend does not hold for compositions with 30 at. % Hf, possibly due to the formation of H-phase particles within the matrix, even with relatively fast water quenching after solution heat treatment [38].

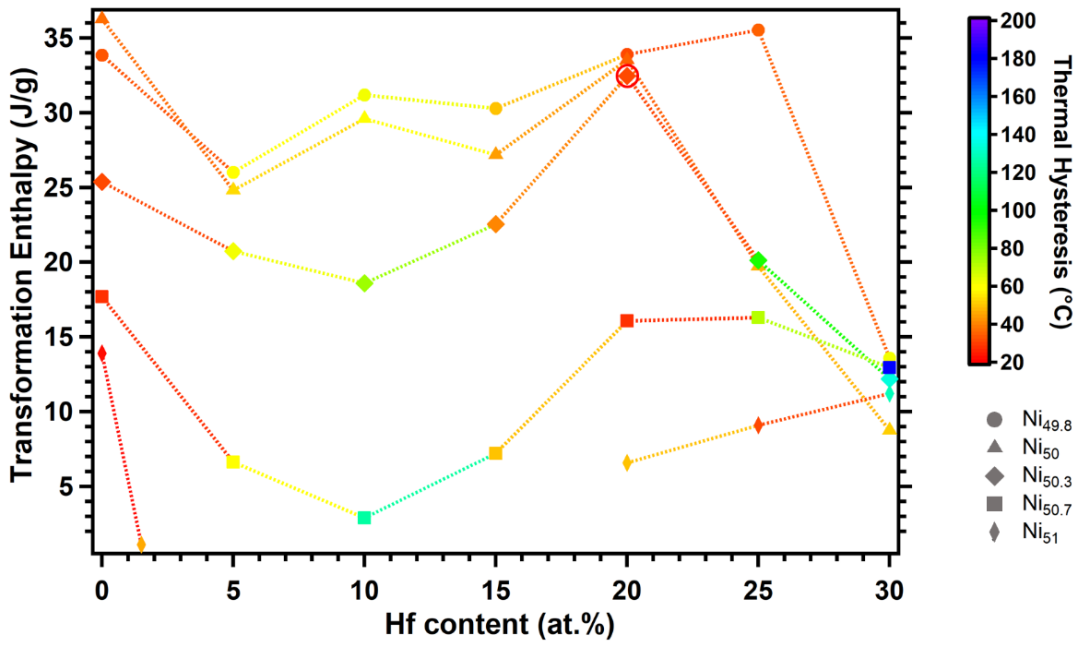

Fig. 2.2. Transformation enthalpies of solution heat treated NiTiHf shape memory alloys are plotted as a function of hafnium content. Each data series, denoted by marker shape, represents alloys of constant Ni content as indicated in the legend. The data point representing the arc-melted $Ni_{50.3}Ti_{29.7}Hf_{20}$ alloy is circled in red. Thermal hysteresis values as reported by Umale et al. [38] are denoted by the color of each maker.

Transformation enthalpies and thermal hysteresis of NiTiHf alloys show strong dependence on Hf content. Hf content dependence of transformation enthalpy demonstrates an inverse relationship to the Hf content dependence of thermal hysteresis. As small amounts of Hf are added to binary NiTi, Hf substitutional defects cause local lattice distortions which create barriers to martensitic transformation. This is reflected in the decreasing transformation enthalpy and increasing thermal hysteresis between 0 at. % and 10 at. % Hf. As Hf content is increased beyond 10 at. %, the increasing unit cell

volume mitigates the local lattice distortions, resulting in decreasing thermal hysteresis and increasing transformation enthalpy between 10 at. % and 20 at. % Hf. The increasing unit cell volume may also result in increased compatibility between the martensite and austenite phases which contributes to lowering thermal hysteresis as has been shown in NiTiHf alloys [30] and NiTi alloys [44]. Above 20 at. % Hf, where there is a local minimum in hysteresis and a local maximum in transformation enthalpy, transformation enthalpy decreases and hysteresis increases significantly upon further Hf addition. Although the reason for this increase in transformation hysteresis is not clear, it may be influenced by the formation of Hf oxides or carbides, formation of H-phase particles even after solution heat treatment and water quenching due to the fast nucleation kinetics [30, 45, 46], and/or strain glass formation at higher Ni contents resulting from large amounts of Hf addition [46].

The strong influence of transformation enthalpies on the FOM of NiTiHf alloys makes this transformation enthalpy map vital in selecting high-FOM NiTiHf alloys. Due to the high transformation enthalpies of $Ni_{49.8}TiHf_{0\text{-}20}$ and $Ni_{50}TiHf_{0\text{-}20}$, these alloys are expected to exhibit high FOM. The observed relationship between NiTiHf composition and thermal hysteresis allows for selection of low-hysteresis NiTiHf compositions; although thermal hysteresis is not a factor in the FOM, a low value is often necessary or advantageous in TES applications as previously discussed.

2.3.3. Alloy Selection for Thermal Conductivity Measurements

The trends in transformation temperature, thermal hysteresis, transformation enthalpy, and density were considered in order to select a NiTiHf alloy composition for bulk fabrication and thermal conductivity measurement. Of the NiTiHf transformation enthalpies measured in this work, $Ni_{50.3}Ti_{29.7}Hf_{20}$ demonstrates one of the highest values at 32.5 J/g, making it an attractive alloy for TES applications. This composition also exhibits one of the lowest thermal hysteresis with 31°C and demonstrates high-temperature transformation with an A_f temperature of 289°C. Due to its high transformation temperature, low thermal hysteresis, and high enthalpy of transformation combination, $Ni_{50.3}Ti_{29.7}Hf_{20}$ was determined to be the most promising composition for the high-temperature TES applications, and a bulk sample was fabricated for further analysis. $Ni_{49.8}Ti_{25.2}Hf_{25}$ was also considered for bulk fabrication due to its high transformation enthalpy, however it was eliminated due to its higher thermal hysteresis and likely poor cyclic stability as has been shown in stoichiometric and Ni-lean NiTiHf compositions [47, 48].

The A_f temperature of the bulk sample was determined to be 193°C using DSC measurements, which is 96°C lower than the A_f temperature of the arc-melted sample of the same nominal composition. This discrepancy indicates a difference in true composition between the samples. The arc-melted sample was measured to have a mass loss of less than 0.1 % after melting and is therefore considered to be accurate in its nominal composition. When compared with the arc-melted sample of composition $Ni_{50.3}Ti_{29.7}Hf_{20}$, the lower transformation temperature of the bulk sample indicates that its

true composition is 0.3 at. % to 0.4 at. % higher in Ni content compared to its nominal composition. This deviation between the nominal and true compositions was confirmed by ICP-AES (inductively coupled plasma atomic emission spectroscopy) composition analysis, which yielded a composition of $Ni_{50.8}Ti_{29.6}Hf_{19.4}$ (the remaining 0.2 % is composed of trace amounts of C, N, O, and Zr).

2.3.4. Specific Heat Capacity and Thermal Conductivity

In order to determine the FOM of the bulk sample, the thermal diffusivity and specific heat capacity (from which thermal conductivity is calculated) were measured. The specific heat capacity values of the bulk $Ni_{50.3}Ti_{29.7}Hf_{20}$ sample as measured by DSC are plotted against temperature in Fig. 2.3. Specific heat capacity slowly increases as temperature increases, followed by a large spike during the transformation. The spike in measured specific heat capacity is attributed to the entropy change during reverse martensitic transformation and is therefore not representative of the true specific heat capacity within the transformation temperature range [49]. After transforming to austenite, the specific heat capacity returned to its pre-transformation level and subsequently decreased slowly as temperature was increased further. This behavior agrees with the trend in specific heat capacity reported in binary NiTi SMA by Cheng *et al.* [50].

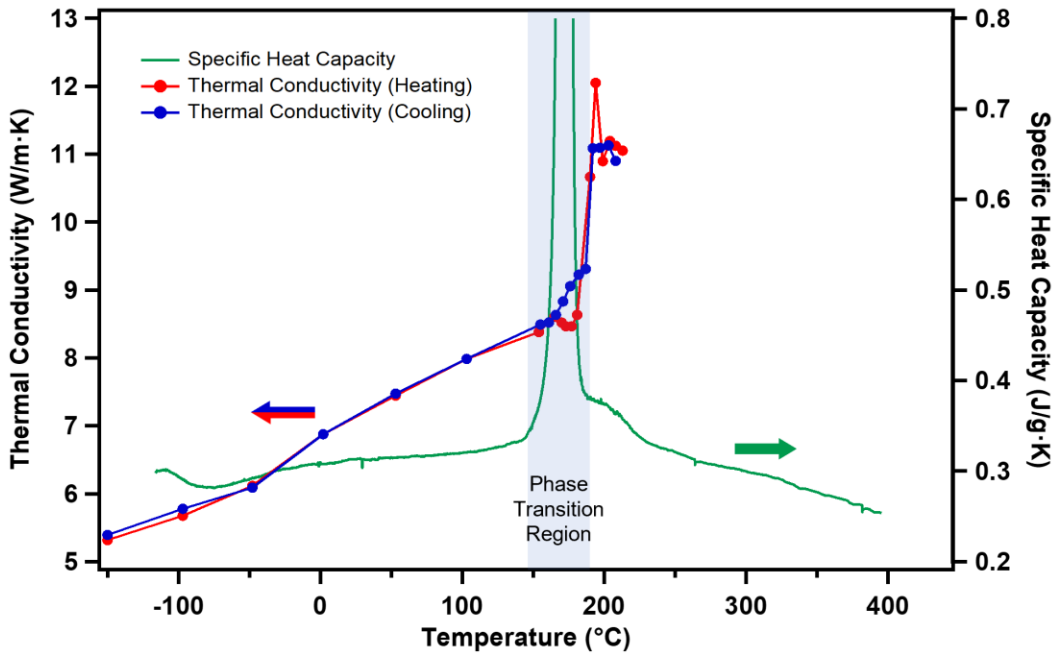

Fig. 2.3. Specific heat capacity and thermal conductivity of $Ni_{50.3}Ti_{29.7}Hf_{20}$ SMA as a function of temperature. Specific heat capacity was measured through DSC and thermal conductivity was calculated from specific heat capacity, density, and thermal diffusivity as measured using laser flash thermal diffusivity method. Measured thermal conductivity data points are represented by circular markers; the red and blue connecting lines serve to guide the eye and do not represent measured data.

The thermal diffusivity of the bulk NiTiHf alloy as measured by laser flash thermal diffusivity analysis was multiplied by the corresponding density and specific heat capacity values to obtain thermal conductivity as a function of temperature (Fig. 2.3). Upon heating, the thermal conductivity of $Ni_{50.3}Ti_{29.7}Hf_{20}$ increased nearly linearly from a value of 5.32 $Wm^{-1}K^{-1}$ at -150°C to a value of 8.38 $Wm^{-1}K^{-1}$ at 154°C, just before reverse martensitic transformation. As the material underwent reverse transformation, thermal

conductivity dipped slightly before rapidly increasing to 12.05 $Wm^{-1}K^{-1}$ at 194°C. Upon further heating to 208°C, the thermal conductivity reduced slightly, resulting in a thermal conductivity of 11.19 $Wm^{-1}K^{-1}$ in the austenite phase. The thermal conductivity peak associated with the reverse martensitic transformation has also been observed in NiTi, NiTiCu, and NiTiFe SMAs and is hypothesized to be a result of phonon mode softening taking place during the transformation [51, 52]. Upon cooling through martensitic transformation, thermal conductivity displayed thermal hysteresis with higher values during the forward martensitic transformation than during reverse transformation, except the peak at 194°C. Outside of the transformation range, thermal conductivity values measured at a given temperature were similar, regardless of whether the sample was undergoing heating or cooling.

2.3.5. Figure of Merit (FOM)

FOM values were obtained for NiTiHf alloys of varying composition as the product of measured density, latent heat of transformation and thermal conductivity values. The thermal conductivity value of the bulk $Ni_{50.3}Ti_{29.7}Hf_{20}$ sample in the high-temperature phase (11.19 $Wm^{-1}K^{-1}$) was assumed for all NiTiHf compositions as an approximation in calculating the FOM values. This was because of the insufficient sample sizes of the arc melted buttons for the thermal diffusivity measurements and difficulty of achieving target compositions in larger induction melted samples. In Fig. 2.4(a), FOM values are plotted as a function of transformation temperature (A_f temperature for SMAs), comparing the performance of NiTiHf against NiTi [4] and a range of traditional solid-

solid, solid-liquid, and composite PCMs [53-62]. Due to its relatively high thermal conductivity and density, NiTiHf outperforms traditional PCMs in terms of FOM by an order of magnitude. Between transformation temperatures of 0 and 400°C, traditional PCMs have FOM values ranging between 40 and 350 while NiTiHf ranges between 500 and 3300 ($10^6 J^2 K^{-1} s^{-1} m^{-4}$). FOM values as high as 800 have been achieved in composite PCMs composed of an organic PCM matrix and a thermally conductive dispersed phase [59-62], however composite fabrication and containment of the liquid phase remain as challenges. In Fig. 2.4(b), volumetric energy storage density is plotted against transformation temperature for NiTiHf, NiTi, and various existing PCMs. The high density and relatively low transformation enthalpy of NiTiHf SMAs result in volumetric energy density values comparable to, but not exceeding those of traditional solid-liquid, solid-solid, and composite PCMs. The primary merit of NiTiHf SMAs as PCMs therefore lies in their solid-solid transformation and high performance in high-power thermal energy storage applications as indicated by their exceptional FOM values. Binary NiTi was shown to have comparable FOM value to some NiTiHf compositions, however NiTiHf is capable of transforming well beyond the 100°C limit which bounds NiTi transformation, and it therefore populates previously empty regions of FOM vs. transformation temperature space. High FOM combined with high and wide-ranging transformation temperatures make NiTiHf an excellent solid-solid PCM candidate for high-temperature applications.

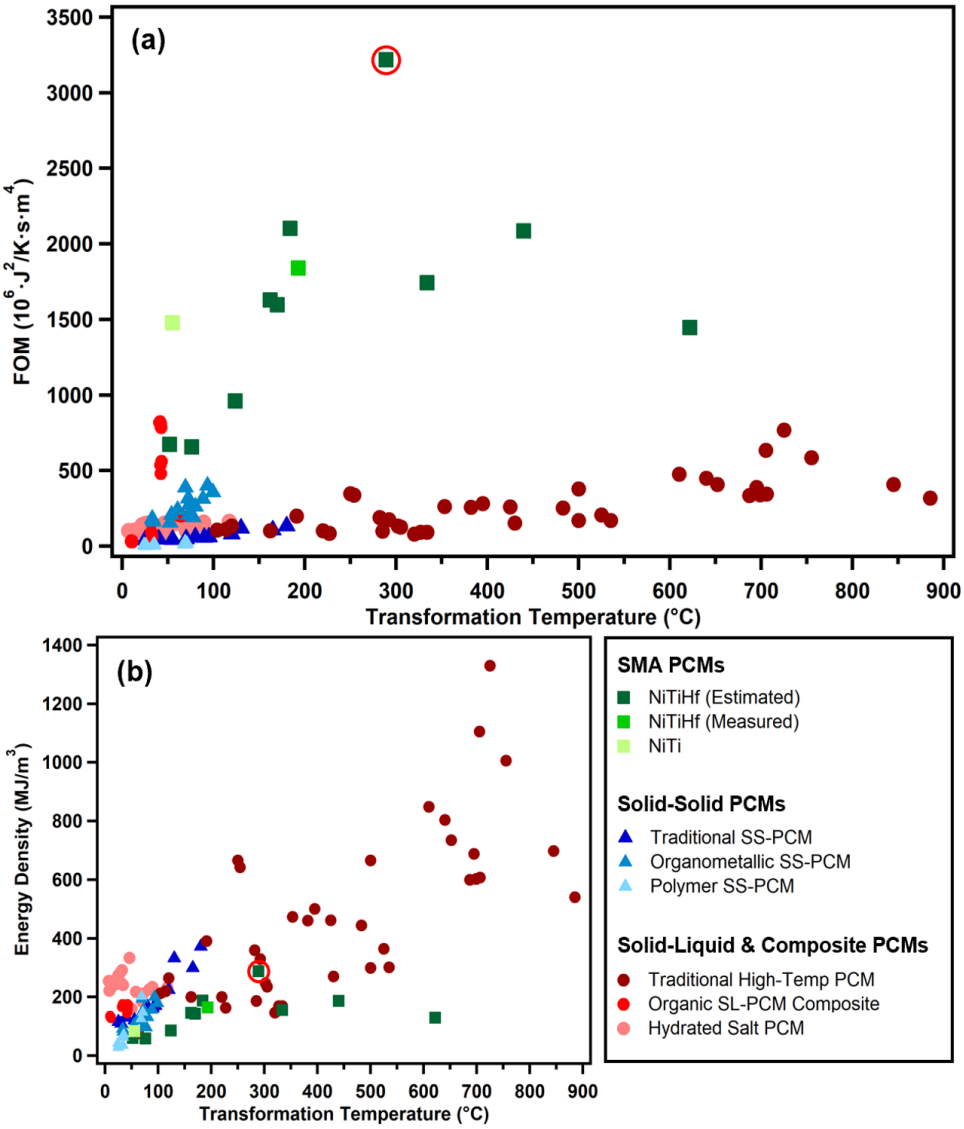

Fig. 2.4. (a) Figure of Merit (FOM) is plotted against transformation temperature, and (b) volumetric energy density is plotted against transformation temperature for NiTi and NiTiHf SMAs, and existing PCMs [4, 53-62]. For SMAs, A_f temperatures are plotted. The medium green marker indicates the bulk NiTiHf composition (nominal composition: $Ni_{50.3}Ti_{29.7}Hf_{20}$, measured composition: $Ni_{50.8}Ti_{29.6}Hf_{19.4}$) with FOM calculated from the measured thermal conductivity, density, and enthalpy of transformation. Dark green

markers represent NiTiHf alloys with FOM calculated based on the thermal conductivity estimated to be equal to that of $Ni_{50.3}Ti_{29.7}Hf_{20}$, and the measured density, and enthalpy of transformation. The data point representing the arc-melted $Ni_{50.3}Ti_{29.7}Hf_{20}$ sample is circled in red.

Fig. 2.5 is a plot of FOM values against thermal hysteresis for NiTiHf alloys. The FOM values for equiatomic NiTi SMA, traditional solid-solid PCMs, and composite PCMs are also included for comparison purposes [4, 56-62]. Corresponding M_s temperatures are represented by the colors of the markers. An ideal PCM is characterized by minimal hysteresis and maximum FOM value, thus the most desirable PCMs are located nearest the upper left-hand corner of the plot. Although NiTi achieves a FOM nearly double that of composite PCMs, its 40°C hysteresis presents a drawback in comparison to the 6-33°C hysteresis of traditional solid-solid and composite PCMs. However, NiTiHf SMAs improve upon the PCM performance of NiTi, demonstrating both lower hysteresis and higher FOM. Of the 11 NiTiHf alloys studied, 5 alloys achieve lower thermal hysteresis, and 7 alloys achieve higher FOM values compared to NiTi. Due to its large latent heat of transformation, $Ni_{50.3}Ti_{29.7}Hf_{20}$ demonstrates the highest FOM value of 3217×10^6 $J^2K^{-1}s^{-1}m^{-4}$ which is 118% higher than the measured FOM value of NiTi: 1478 $10^6 J^2K^{-1}s^{-1}m^{-4}$ [4]. $Ni_{51.2}Ti_{18.8}Hf_{30}$ registered the lowest thermal hysteresis of the NiTiHf alloys at 22°C and possesses a relatively high FOM value of 1629 $10^6 J^2K^{-1}s^{-1}m^{-4}$. As shown in the upper left-hand corner of Fig. 2.5, 5 NiTiHf alloys exhibit both higher FOM and equal or lower thermal hysteresis as compared to binary NiTi ($Ni_{50.3}Ti_{34.7}Hf_{15}$,

$Ni_{50.3}Ti_{29.7}Hf_{20}$, $Ni_{50.7}Ti_{29.3}Hf_{20}$, $Ni_{51.2}Ti_{18.8}Hf_{30}$, and $Ni_{50.8}Ti_{29.6}Hf_{19.4}$ (bulk alloy, measured composition)).

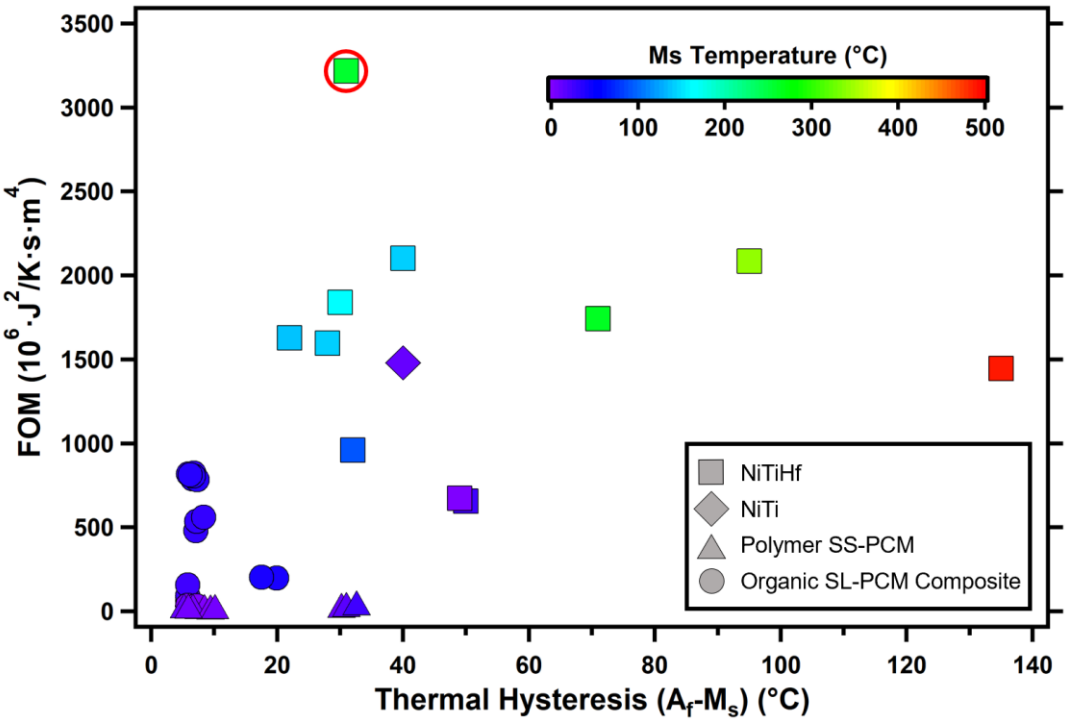

Fig. 2.5. Figure of merit (FOM) is plotted against thermal hysteresis of binary NiTi [4], NiTiHf alloys of varying composition, and existing PCMs [56-62]. M_s temperatures are indicated by the color of each marker. The data point corresponding to $Ni_{50.3}Ti_{29.7}Hf_{20}$ is circled in red. Thermal hysteresis of the binary NiTi alloy was not reported in [4], and was therefore estimated based on the measured thermal hysteresis of a NiTi alloy of similar transformation temperatures [63].

2.4. Summary and Conclusions

NiTiHf shape memory alloys demonstrate considerable promise as high-temperature solid-solid PCMs. The well-mapped relationship between composition and transformation temperatures enables tunability of NiTiHf alloys to specific TES applications including those with operation temperature requirements well in excess of the 100°C limitation of binary NiTi. In terms of PCM performance, NiTiHf shows FOM values up to 10 times the values displayed by traditional PCMs (hydrated salts, organics, inorganics, and other commercially available PCMs), populating previously empty regions of hysteresis–FOM–space and transformation–temperature–FOM–space. NiTiHf alloys improve upon the recent establishment of NiTi SMA as an effective PCM by demonstrating lower hysteresis, higher temperature capability, and more than double the FOM value of binary NiTi. Furthermore, the trends in the density and transformation enthalpy of NiTiHf with respect to composition allow for further tuning and optimization of FOM values in NiTiHf alloys. Although NiTiHf alloys yield significant improvements in FOM and transformation temperatures compared to NiTi, improvements in thermal hysteresis are modest, and therefore in future works, alternative SMA systems should be studied in search of alloys demonstrating high FOM combined with even lower thermal hysteresis. After promising alloy systems are identified, understanding the influence of composition and thermomechanical processing on thermophysical properties of SMA PCM candidates will allow for optimization of PCM performance within alloy systems.

3. IDENTIFICATION AND DESIGN OF NITICU SHAPE MEMORY ALLOYS WITH SMALL OVERALL TRANSFORMATION RANGE FOR PHASE CHANGE MATERIAL APPLICATIONS

3.1. Introduction

Shape memory alloys (SMAs) have recently been demonstrated as effective solid-solid phase change materials (PCMs) in thermal energy storage and thermal management applications [4, 10, 64]. The endothermic reverse martensitic transformation of SMAs allows them to function similarly to traditional solid-liquid PCMs, absorbing large amounts of heat while maintaining nearly constant temperature. This is demonstrated in Fig. 3.1 which depicts a characteristic heat flow vs. temperature curve of a PCM undergoing melting and recrystallization, or equivalently, an SMA undergoing reverse and forward martensitic transformation in an example thermal management application. At Step 1, the system operates at steady state, with the waste heat from the electronic chip being dissipated by conduction through the PCM/SMA and subsequently by convection to the surrounding air. When the power supplied to the chip is increased during Step 2, heat flow into the PCM/SMA is increased, causing it to undergo sensible heating. At the beginning of Step 3, the PCM reaches its melting onset temperature (austenite start temperature – A_s – for SMAs) and the rate of the temperature increase decreases significantly due to the latent heat absorbed by the PCM (often referred to as transformation enthalpy within the context of SMAs). As the PCM continues to absorb heat from the electronic chip, its temperature remains relatively constant until the latent

heat is exhausted and the melting endpoint temperature (austenite finish temperature – A_f – for SMAs) is reached. At this point, a traditional PCM is fully in the liquid phase, and a SMA is fully in the austenite phase. During Step 4, the power supplied to the chip is reduced to its baseline level, allowing the PCM/SMA to cool sensibly until it reaches its crystallization onset temperature (martensite start temperature – M_s – for SMAs). As the PCM continues to transfer its stored thermal energy to the surroundings, it reaches its martensitic crystallization endpoint temperature (martensite finish temperature – M_f – for SMAs), "resetting" the phase transformation. At this point, a traditional PCM has fully transformed back to the solid phase, and a SMA has fully transformed back to the martensite phase. The chip can then operate at steady state until high-power operation is again needed, at which time the cycle is repeated. In this way, PCM/SMAs can be used to reduce maximum temperatures experienced during power spikes as shown in the inset in the corner of Fig. 3.1, and as demonstrated experimentally by Sharar et al.[4]

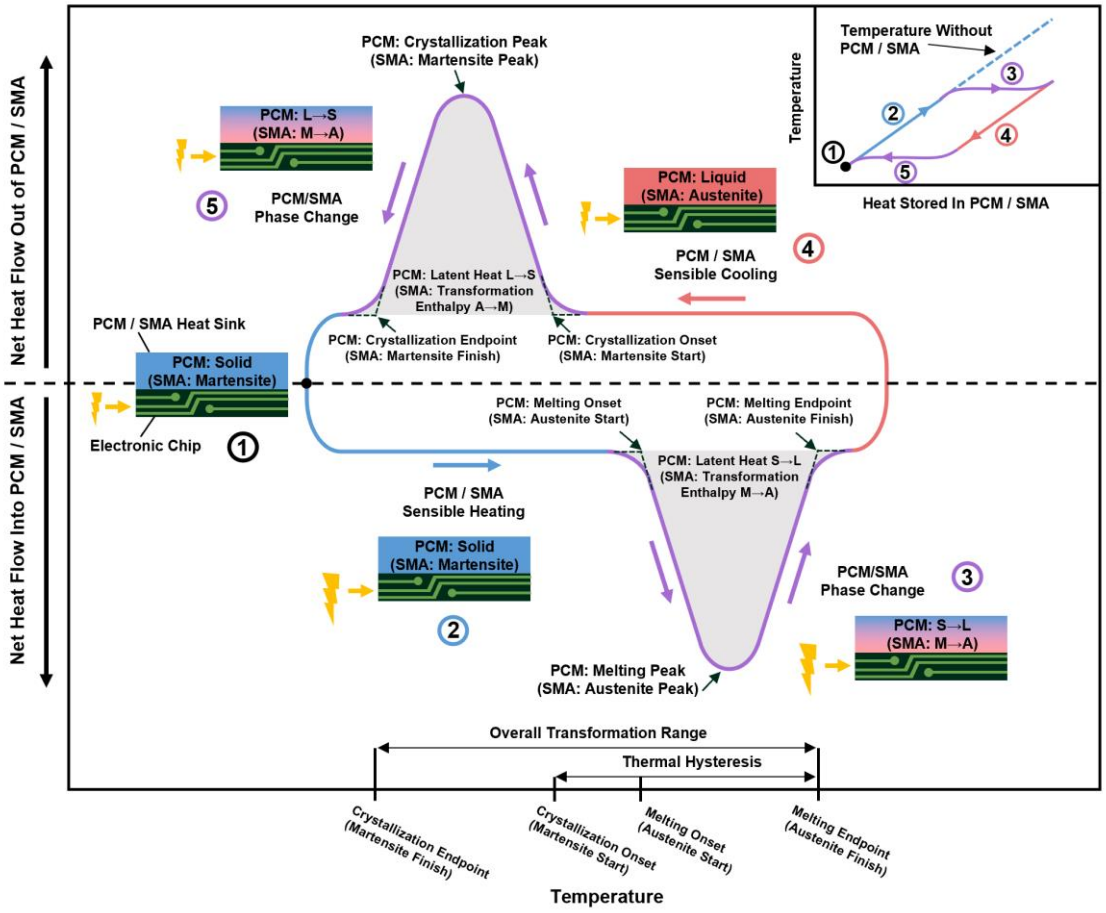

Fig. 3.1. Representative heat flow vs. temperature curve, shown as if measured by differential scanning calorimetry, illustrating typical behavior of PCMs undergoing melting and recrystallization, or equivalently, SMAs undergoing reverse and forward martensitic transformation in a thermal management application. PCM transformation temperatures are labeled with typical nomenclature, and equivalent corresponding transformation temperatures of SMAs are labeled in parenthesis. The effect of thermal management via PCM/SMA implementation on system temperature is represented in the inset at top-right.

Traditional organic and inorganic PCMs have been used in many thermal energy storage (TES) and thermal management applications including building temperature regulation, solar air and water heating systems, battery thermal management, space applications, and microelectronic thermal management [1]. Despite the many uses of traditional PCMs, their low thermal conductivity, typically 0.1-0.7 W/m·K [3], limits their use in applications where fast transient thermal transport is required (for example, microelectronic thermal management as depicted in Fig. 3.1). By comparison, SMAs have thermal conductivity values 1-2 orders of magnitude greater than traditional PCMs, making them good candidates for such applications. In order to identify the optimal PCM for fast transient thermal management applications, Lu derived a figure of merit (FOM) which quantifies the ability of a PCM to absorb a heat pulse as $FOM = \rho \cdot L \cdot k$, where ρ is density, L is latent heat of transformation, and k is thermal conductivity [2]. It has been shown that NiTi [4] and NiTiHf [64] SMAs, in part due to their relatively high thermal conductivities, have FOM values an order of magnitude greater than those of traditional PCMs, making SMAs preferable in high-heat flux thermal management and thermal storage applications. Furthermore, in contrast to traditional PCMs such as salt hydrates, polymers, paraffin, and other organics, SMAs remain solid throughout their transformation, eliminating the need for fluid containment as is necessary for traditional solid-liquid PCMs. In recent works, the thermal conductivities of traditional PCMs have been increased by adding a conductive dispersed phase [59-62], however the FOM values of these composite PCMs are typically less than 800 $10^6 \cdot J^2/K \cdot s \cdot m^4$ [59-62] compared to SMAs which have FOM values ranging up to 3200 $10^6 \cdot J^2/K \cdot s \cdot m^4$ [4, 10, 64]. The

implementation of composite PCMs is further hindered by difficult fabrication procedures and the need for containment of the liquid phase which adds size and weight to the system which does not directly contribute to the thermal energy storage process. Traditional solid-solid PCMs show even lower FOM values, typically less than 140 $10^6 \cdot J^2/K \cdot s \cdot m^4$ [3].

Despite the advantages provided by the high FOM values and solid-solid transformations of NiTi and NiTiHf SMAs, both alloys have large overall transformation range (OTR, given by A_F-M_F) in excess of 50°C, excluding them from some applications [64, 65]. As an example, some solid-state lasers may be limited to operation temperature ranges as narrow as 10°C, and therefore corresponding PCM thermal management solutions must undergo full forward and reverse transformations within these narrow temperature windows [8]. Regardless of application temperature range requirements, lower OTRs in PCMs are preferable because they allow for increased thermal cycling frequency and therefore a higher number of heat pulses can be absorbed within a given length of time. Low OTRs are especially important in SMAs in thermal cycling applications, as observed latent heat is maximized with complete austenite and martensite transformation. Furthermore, the temperature memory of SMAs degrades with partial cycling, which could lead the operating temperature of the SMA to shift outside of the objective temperature range [66, 67]. Thus, in order to optimize a SMA for thermal storage and management applications, minimization of the OTR is necessary to ensure transformation is completed within the application temperature constraints. Therefore, an evaluation of the material parameters affecting OTR and transformation temperatures is needed.

While OTR in SMAs is a function of frictional resistance to interfacial motion similar to thermal hysteresis, it is also a function of the elastic strain energy stored during martensitic transformation and its dissipation [68]. By reducing the density of defects in an SMA, the frictional resistance to motion of transforming phases can be decreased. To minimize the dissipation of the stored elastic strain energy, the crystallographic compatibility between martensite and austenite phases must be improved [69]. Based on the geometric nonlinear theory of martensite, crystallographic compatibility can be qualitatively described by the middle eigenvalue (λ_2) of the transformation stretch tensor between austenite and martensite lattices. The closer λ_2 is to a value of 1, the better the compatibility between the austenite-martensite interfaces during transformation and thus the lower chance of defect formation [69-74]. Finally, reducing the amount of stored elastic strain energy can be accomplished by reducing defect density and precipitate coherency strains [68]. In the absence of defects such as dislocations and precipitates, martensitic transformation is nucleation controlled, propagating instantly through the material upon reaching critical nuclei size [75]. Chemical homogeneity throughout a sample is also important as the transformation temperatures are sensitive to small changes in composition [65]. Chemical homogeneity will ensure the martensitic transformation occurs at a given temperature simultaneously throughout the entirety of the material within a narrow temperature range.

In NiTi-based SMAs, Cu, Pd, Au, and Cr elemental additions can result in a smaller OTR than other NiTi-based SMAs [25, 69, 71, 76-79], and of these elemental additions, Cu and Pd have the greatest effect on minimizing the OTR [25, 74, 78-82] due

to the enhanced crystallographic compatibility. However, the composition and processing parameters in a given NiTi-X system can greatly affect the observed OTR. These differences can be seen in NiTiCu alloys as shown by the adapted DSC plots from literature in Fig. 3.2(a). Other adapted DSC plots demonstrating similar behavior in NiTi, NiTiHf, and NiTiPd can be seen in the supplementary materials (Fig. 7.1). The offset of martensite and austenite peaks, characterized by A_S-M_S, and the entire OTR, A_F-M_F, is used to determine candidate alloys, shown in Fig. 3.2(b). The smallest OTRs occur in compositions that are capable of single step B2-B19 phase transformations (more commonly reported in NiTiCu and NiTiPd), rather than B2-B19' or multi-step B2-B19-B19' phase transformations (more commonly reported in NiTi and NiTiHf). In order to achieve the minimum OTR, the ideal SMA would have characteristically sharp martensite and austenite DSC peaks that have minimal peak offset, indicating both austenite and martensite phase transformations occur rapidly with temperature change and within the same temperature range throughout the sample. In addition to minimal amount of stored elastic energy in an alloy, from compiled literature data shown in Figure 3.2(b), the SMA compositions with small OTR and with positive peak offset show the greatest potential for achieving minimal OTR. This can be achieved by reducing the peak offset through altering composition and processing parameters. From Figure 3.2(b), the candidate alloys are predominately NiTiCu compositions.

To this end, the present work focuses on determining and optimizing the potential thermal energy storage application of the NiTiCu SMA system by synthesizing 24 NiTiCu alloys, changing Ni and Cu content to investigate the effect of composition on martensitic

transformation temperatures and the OTR in bulk material. The NiTiCu system has been heavily studied for alloys where Ti is near or greater than 50 at.% [74, 83], however, little has been shown for bulk NiTiCu for Ti less than 50 at.% [84]. The effect of Ni and Cu concentration on secondary phase formation was also studied to better understand microstructural evolution and its effect on martensitic transformation, thermophysical properties, and PCM performance. In comparison to traditional solid-liquid PCMs, solid-solid phase transformations in SMAs with small OTRs will offer a unique solution for thermal energy absorption and management applications.

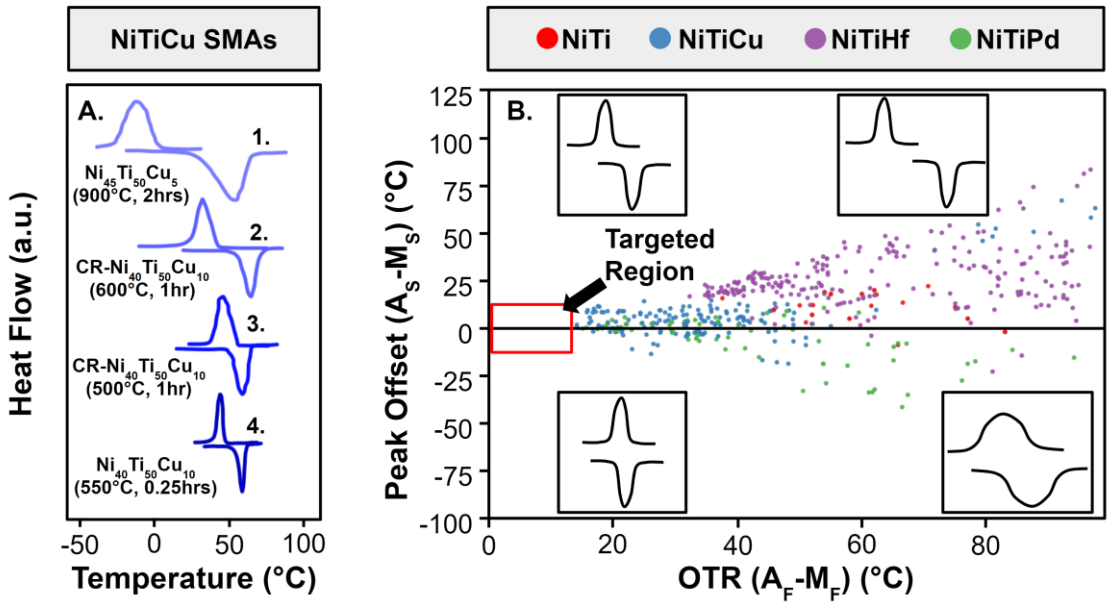

Fig. 3.2. (a) Adapted DSC plots from literature for solution treated $Ni_{45}Ti_{50}Cu_5$ (1 - Chang et al [85]), cold rolled and annealed $Ni_{40}Ti_{50}Cu_{10}$ (2 - Nam et al [86], 3 - Lin et al [87]), and annealed $Ni_{40}Ti_{50}Cu_{10}$ wire (4 – Bertacchini [88]) samples. (b) Scatter plot of OTR versus peak offset for NiTi, NiTiHf, NiTiPd, and NiTiCu from literature [25, 38, 71, 73, 75, 89-112]. R-phase martensitic transformations are not included.

3.2. Results and Discussion

In order to evaluate the NiTiCu system for various application temperatures, 24 NiTiCu samples were synthesized using a full-factorial design of experiments to investigate the combinatorial $Ni_{100-X-Y}Ti_XCu_Y$ composition space, where X = [40, 42, 44, 46, 48, 50] and Y = [20, 22.5, 25, 30]. The compositional space explored in this study is visualized in the ternary diagram in Fig. 3.3. The 24 alloys have high Cu content (>20 at.%), where, based on previous studies [113], the expected transformation in these alloys

is single stage B2-B19 transformation. After fabrication and heat treatment of the 24 NiTiCu samples, the microstructures were studied in SEM. A representative microstructure can be seen in the supplementary materials (Fig. 7.2). A second phase, which is $(Cu,Ni)_2(Ti)$ according to the NiTiCu phase diagram [114], was only observed in alloys where Ti<50 at.%. In addition, black precipitates were observed in SEM/EDX and were identified to be $Ti_2(Ni,Cu)$. The composition distributions from EDX can be found in the supplementary materials (Fig. 7.3).

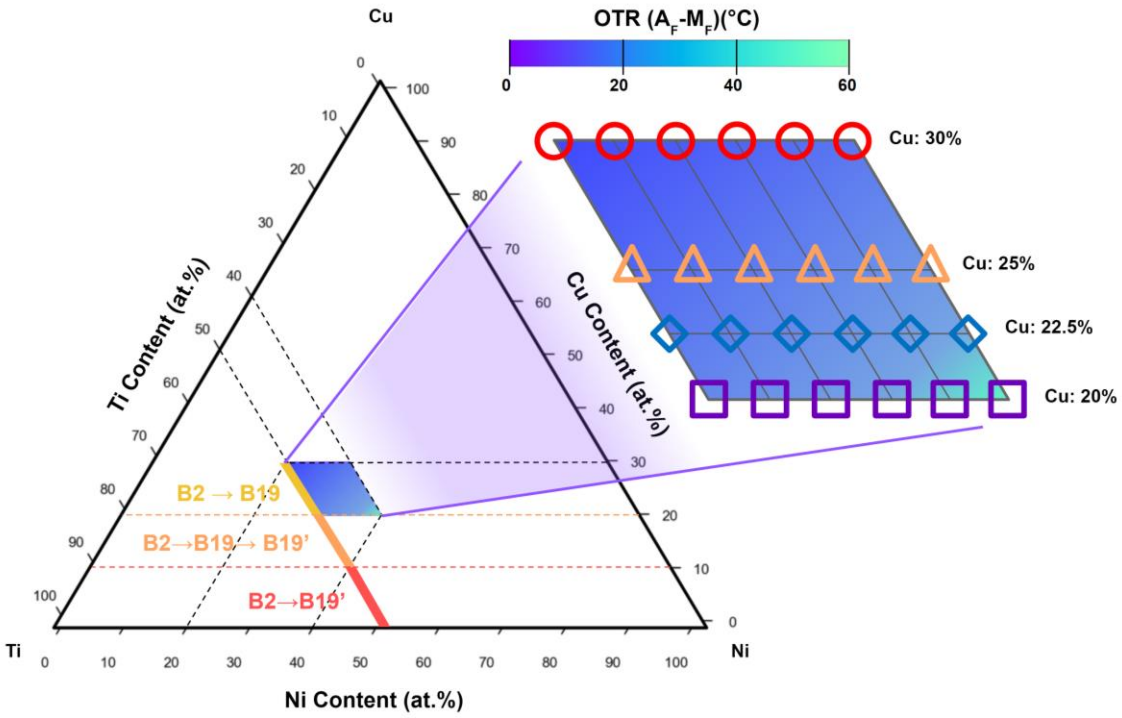

Fig. 3.3. NiTiCu Ternary Diagram with highlighted grid selected for testing. Red dashed line at Cu=10 at.% and orange dashed line at Cu=20 at.% separate the composition space into three regions, indicating preference of single stage B2-B19' (0 < Cu at.% < 10), two

stage B2-B19-B19' (10 < Cu at.% < 20), and single stage B2-B19 (20 < Cu at.% <30), martensitic transformations [113].

The DSC results of the NiTiCu samples demonstrate clear martensitic transformation peaks (DSC for $Ni_XTi_{75-X}Cu_{25}$ shown in Fig. 3.4(a)) with excellent cyclic stability of transformation (Fig. 3.4(b)). The NiTiCu system is known for excellent transformation stability [105, 115-117], and the very small changes in the martensite and austenite peaks for each cycle in this work are among the smallest reported in NiTi-based SMAs. After 20 heating-cooling cycles, the transformation peaks of $Ni_{29}Ti_{46}Cu_{25}$ and $Ni_{27}Ti_{48}Cu_{25}$ each shifted by only 0.06°C (measured at the midpoint of the low-temperature slope of the austenite to martensite peak), and the alloys retained 99.6% and 99.3% of their first-cycle transformation enthalpies, respectively. For comparison, Zarnetta et al. demonstrated the cyclic stability of $Ni_{50}Ti_{50}$, $Ni_{50}Ti_{35}Cu_{15}$, and $Ni_{50}Ti_{39}Pd_{11}$, with the alloys showing transformation peak shifts after 20 thermal cycles of 12.5, 0.65, and 0.39°C respectively [118] (measured in the same manner as in this study). $Ni_{50.2}Ti_{34.4}Cu_{12.3}Pd_{3.1}$ showed greater cyclic stability than the other alloys from the study, with a temperature shift of 0.1°C after 80 thermal cycles [118]. The transformation temperatures A_f and M_f and are plotted as a function of composition in Fig. 3.4(c) and Fig. 3.4(d). An initial sharp decrease in transformation temperatures is observed upon decreasing Ti content below 50 at.%, followed by smooth descent in transformation temperatures with further decrease in Ti content. The OTRs of these alloys are plotted in Fig. 3.4(e) which shows a sharp increase in OTR occurring when Ni>35 at.%. The

transformation temperatures for the third cycle from each composition can be found in Table 3.1. The OTR, A_f, and M_f temperatures versus the Ni content confirmed by EDX can be found in the supplementary materials (Fig. 7.3(c) and 7.3(d)).

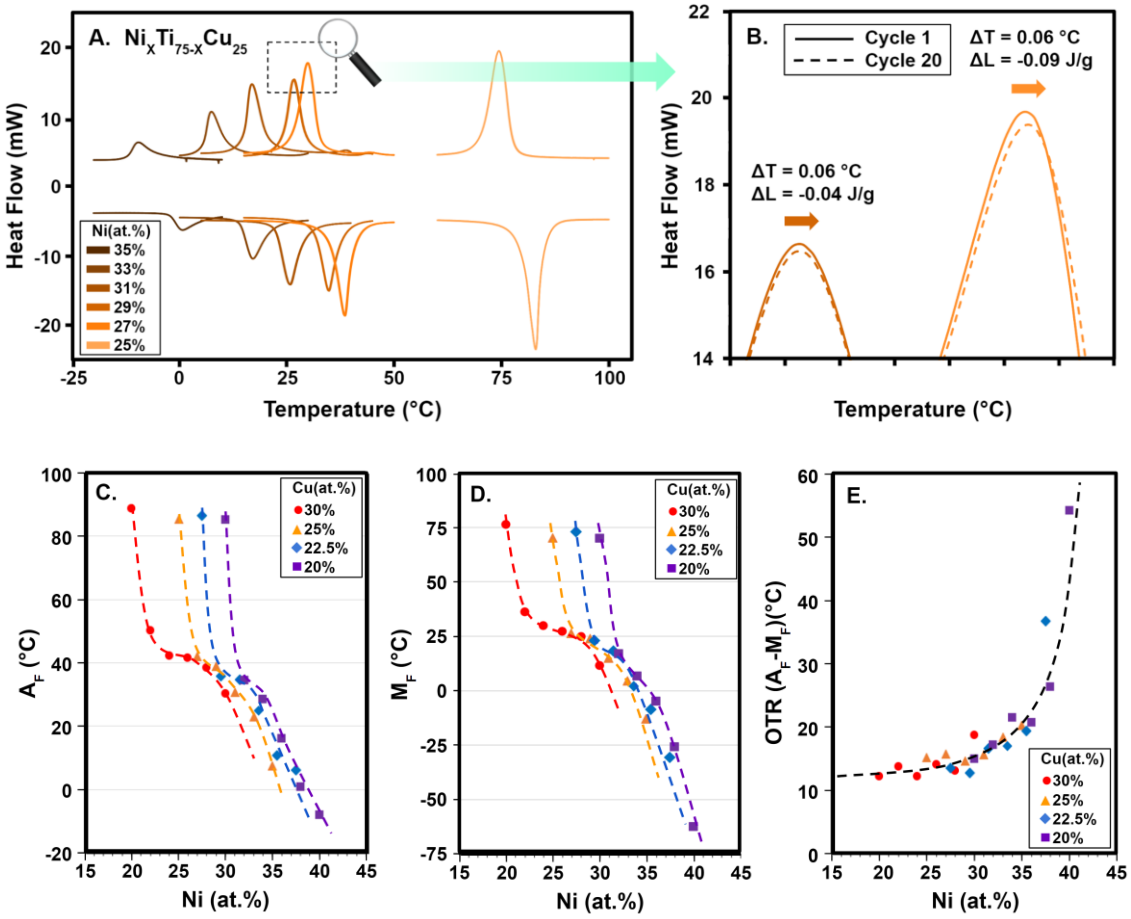

Fig. 3.4. Differential Scanning Calorimeter results for 3 heating and cooling cycles for $Ni_XTi_{75-X}Cu_{25}$ (a) and a magnified view of the austenite to martensite peaks illustrating excellent thermal cycling stability (b). All compositions are compared for Austenite Finish (A_f) temperature (c), Martensite Finish (M_f) temperature (d), and OTR (A_f-M_f) (e) with respect to Ni content for NiTiCu SMAs, colored by the Cu content.

Table 3.1. All compositions presented in this study with the analyzed Differential Scanning Calorimetry data for the 3rd thermal cycle. This includes transformation temperatures, peak offset (A_s-M_s), OTR (A_f-M_f), and the latent heat of transformation for martensite to austenite (ΔH_{MA}) and austenite to martensite (ΔH_{AM}).

Ni	Ti	Cu	M_f	M_p	M_s	A_s	A_p	A_f	A_s-M_s	A_f-M_f	ΔH_{MA}	ΔH_{AM}
30.0	40.0	30.0	11.6	15.9	22.3	18.8	22.6	30.3	-3.5	18.7	4.0	3.9
28.0	42.0	30.0	25.3	28.0	31.1	30.9	33.6	38.4	-0.2	13.1	5.6	5.4
26.0	44.0	30.0	27.4	33.3	35.6	34.5	37.7	41.5	-1.1	14.1	6.8	6.6
24.0	46.0	30.0	30.0	36.5	38.6	38.6	40.3	42.2	0	12.2	8.8	9.5
22.0	48.0	30.0	36.4	40.5	44.2	42.8	45.3	50.1	-1.4	13.7	12.0	12.4
20.0	50.0	30.0	76.5	81.1	83.8	83.6	85.6	88.7	-0.2	12.2	15.5	15.4
35.0	40.0	25.0	-12.8	-9.6	-4.2	-2.1	0.6	7.5	2.1	20.3	3.5	3.7
33.0	42.0	25.0	4.5	7.9	11.7	14.1	16.6	22.9	2.4	18.4	5.6	5.5
31.0	44.0	25.0	15.2	17.6	20.8	22.3	24.9	30.8	1.5	15.7	7.5	7.5
29.0	46.0	25.0	24.2	27.4	29.7	31.3	33.8	38.8	1.6	14.6	9.1	9.0
27.0	48.0	25.0	26.2	30.8	32.7	34.9	37.2	41.9	2.2	15.7	11.6	11.6
25.0	50.0	25.0	70.2	75.5	77.6	79.5	81.5	85.4	1.9	15.2	14.6	14.6
37.5	40.0	22.5	-30.6	-24.1	-4.5	-18.9	-12.4	6.2	-14.4	36.8	2.6	2.8
35.5	42.0	22.5	-8.6	-5.5	-0.8	1.6	4.4	10.8	2.4	19.4	5.2	5.3
33.5	44.0	22.5	6.5	12.1	14.0	14.2	17.4	23.2	0.2	16.7	6.7	6.7
31.5	46.0	22.5	18.2	21.4	24.5	26.1	29.3	34.8	1.6	16.6	8.8	8.6
29.5	48.0	22.5	23.0	26.8	28.6	31.5	33.5	35.7	2.9	12.7	10.6	10.8
27.5	50.0	22.5	73.1	77.9	80.3	81.5	83.7	86.6	1.2	13.6	16.7	16.7
40.0	40.0	20.0	-62.3	-47.1	-22.2	-49.4	-30.7	-8.1	-27.2	54.2	3.2	2.9
38.0	42.0	20.0	-25.6	-20.8	-12.1	-13.5	-8.9	0.7	-1.4	26.3	4.8	5.0
36.0	44.0	20.0	-4.6	-1.6	4.7	4.5	8.4	16.1	-0.2	20.7	6.8	6.8
34.0	46.0	20.0	6.9	12.8	17.5	16.1	21.3	28.4	-1.4	21.5	9.3	9.1
32.0	48.0	20.0	17.2	20.7	23.3	26.3	28.8	34.4	3	17.2	11.9	11.9
30.0	50.0	20.0	70.3	75.5	78.3	79.1	82.5	85.2	0.8	14.9	16.7	16.4

Composition is in at.%, Transformation Temperatures are in °C, and Latent Heat of Transformation is in J/g.

The slow cooling rate after homogenization likely contributed to the small OTR in the NiTiCu samples. It has been shown in both NiTi-based [119] and Cu-based [120] SMAs that thermal hysteresis is dependent on quench media, with rapid cooling rates yielding an increase in defect generation and an increase in thermal hysteresis, and thus OTR. In a high-throughput study on thin film NiTiCu alloys, Zarnetta et al. [80] reported that thermal hysteresis had a negative correlation with annealing temperature, with the smallest resulting OTR in the $Ti_{50}Ni_{50-x}Cu_x$ stoichiometric compositions at an annealing temperature of 700˚C. They reported that the coarsening of precipitate phases such as Ti-rich and (Ni, Cu)-rich phases were responsible for the observed decrease in thermal hysteresis. However, they only reported heat treatments of up to 700˚C for 1 h. The high temperature homogenization treatment used in this study (925˚C) as well as longer treatment time (48 h) likely resulted in coarser precipitates, reducing the amount of stored elastic energy and contributing to the small OTRs observed. It is also possible that the homogenization treatment followed by air cooling allowed for a close-to-equilibrium microstructure to form, as opposed to an as-cast or solution treated material, contributing to the overall cyclic stability of the material.

The latent heat of transformation values for the martensite to austenite transformation (listed in Table 3.1) were calculated from the area under the DSC peaks and plotted against the area fraction of second phase, as found using backscattered electron (BSE) images of the samples that can be seen as insets in Fig. 3.5. The latent heat of transformation has a decreasing linear relationship with the area fraction of second phase (lighter region) in the materials (Fig. 3.5(a)). This is, in part, because the second phase

replaces a portion of the transforming material, resulting in a lower amount of transforming material within a bulk sample, and therefore a lower overall latent heat is measured in the sample. However, the percentage decrease in latent heat is of greater magnitude than expected based on the decrease in the mass fraction of transforming material alone, indicating that there is another contributing factor. After normalizing the latent heat by the mass fraction of transforming material, there remains a decreasing trend in latent heat versus the second phase area fraction (Fig. 7.4(a)) with no correlation to the transforming matrix composition (Fig. 7.4(b)). The remaining trend in normalized latent heat with respect to second phase area fraction may be an effect of the confinement of martensitic domains by the second phase, reducing the number and size of martensitic variant formation.

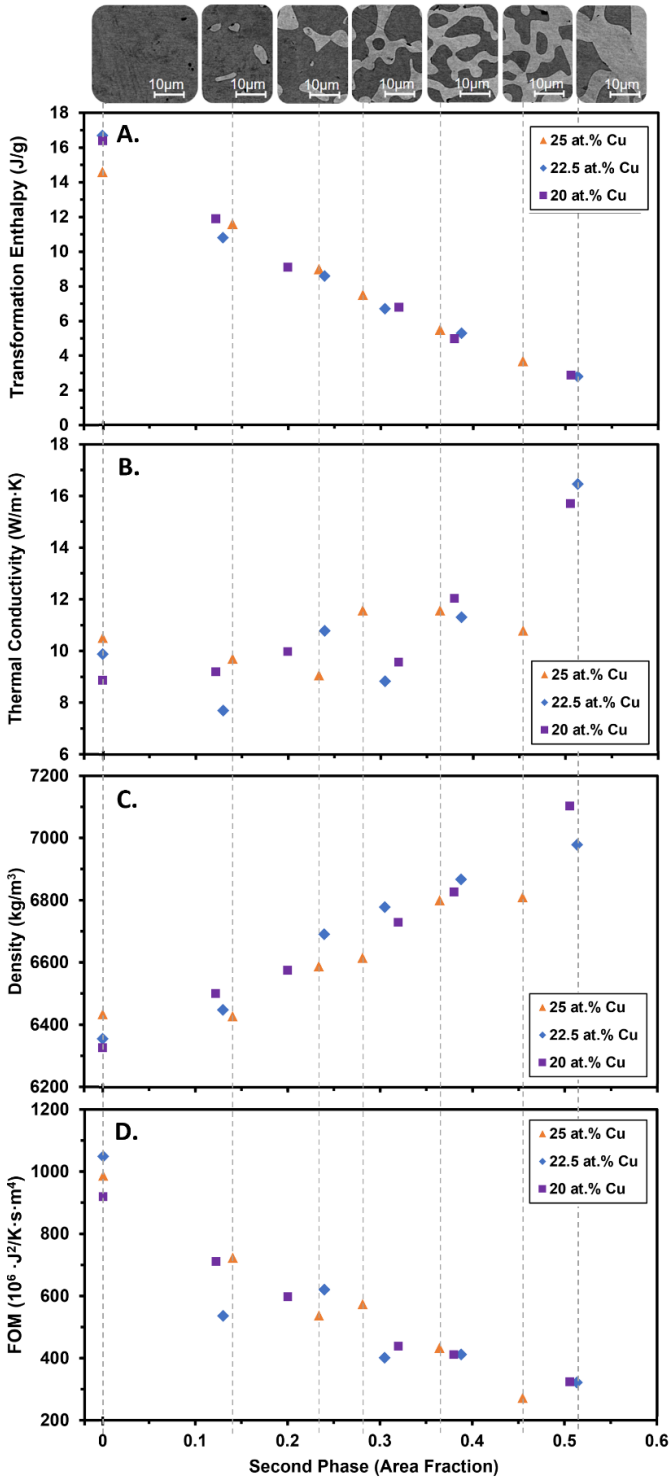

Fig. 3.5. Transformation enthalpy (a), thermal conductivity (b), density (c), and FOM (d) are plotted against second phase area fraction for NiTiCu alloys of varying composition.

Inset images of microstructure show the evolution of second phase. The Ni content generally increases from left to right.

Thermal conductivities of the alloys (Cu = 20, 22.5, 25 at.%) measured at approximately 100°C in the austenite phase are plotted as a function of second phase area fraction in Fig. 5B. Between 0 and 15% second phase, thermal conductivity remains relatively constant between 7.7 and 10.5 W/m·K. As the second phase area fraction increases further, thermal conductivity follows an upward trend, reaching a maximum value of 16.5 W/m·K at just over 50% second phase. This increasing trend indicates that the thermal conductivity of the second phase is higher than that of the austenite phase, contributing to a higher effective thermal conductivity as measured in the bulk material. The nearly constant thermal conductivity measured in the bulk material between 0 and 15% second phase may be attributed to competing factors which negate the effects of one another. The thermal conductivity is positively affected by the addition of a more conductive second phase but negatively affected by phonon scattering at the phase boundaries [121]. The thermal conductivities of the Cu = 30 at.% samples were not tested as the trend in thermal conductivity with respect to second phase was already well established. The specific heat capacities of the alloys in the austenite phase were measured to be between 0.33 and 0.50 J/g·K, however no correlation was found with respect to alloy composition or second phase area fraction.

In Fig. 3.6, the temperature dependent behavior of thermal conductivity and specific heat capacity in $Ni_{25}Ti_{50}Cu_{25}$ are shown. Beginning at -75°C in the martensite

phase, thermal conductivity increased with temperature up to the start of the transformation region. After transformation to the austenite phase, thermal conductivity continued to increase with rising temperature at a similar rate as in the martensite phase. Specific heat capacity increased gradually between -75°C and the transformation region, spiked sharply during transformation, and decreased below the martensite specific heat capacity level upon completing transformation to austenite. The large spike in measured specific heat capacity observed within the transformation region is a result of the latent heat of transformation, and therefore cannot be attributed to sensible heating. The behaviors of thermal conductivity and specific heat capacity observed in this work are similar to those measured in $Ni_{50}Ti_{40}Cu_{10}$ by Ingale et al. [51] Because all of the studied NiTiCu alloys showed similar temperature dependent thermophysical property behavior, the trends shown for $Ni_{25}Ti_{50}Cu_{25}$ in Fig. 3.6 are representative of the other alloys.

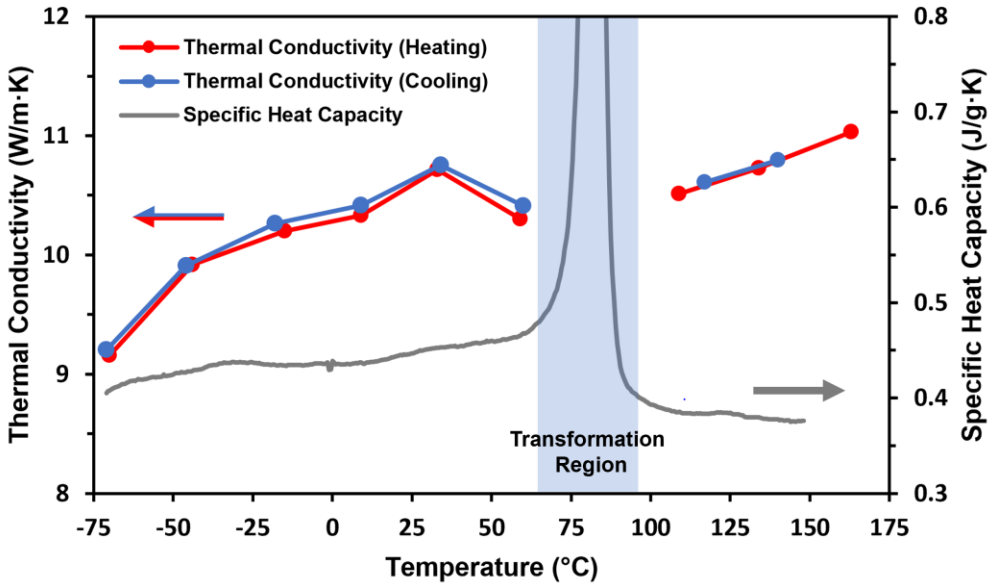

Fig. 3.6. The thermophysical properties of $Ni_{25}Ti_{50}Cu_{25}$ are plotted as a function of temperature. Thermal conductivity was measured during heating (red) and cooling (blue). Specific heat capacity measured during heating is shown in grey.

As with transformation enthalpy and thermal conductivity, the densities of the alloys showed a strong correlation with second phase area fraction as shown in Fig. 3.5(c). Density was found to increase linearly from below 6400 kg/m^3 at 0% second phase to over 7100 kg/m^3 at 50% second phase. Taking the product of the transformation enthalpy (Fig. 5A), thermal conductivity (Fig. 3.5(b)), and density (Fig. 3.5(c)), the FOM of the alloys is obtained as a function of second phase area fraction as shown in Fig. 3.5(d). Despite density and thermal conductivity both showing positive correlations with second phase area fraction, the FOM decreases with increasing second phase area fraction, indicating that FOM is dominated by the decreasing trend in transformation enthalpy. The reason for this is apparent when considering that the highest transformation enthalpy value is 6 times

the lowest value, however thermal conductivity and density only vary by a factor of 2 and 1.2, respectively. From the trend shown in Fig. 3.5(d), it is apparent that PCM performance in NiTiCu SMAs as quantified by FOM can be optimized by selecting compositions near 50% Ti, containing no second phase. For applications in which high thermal conductivity is most important, thermal conductivity can be increased to desired levels by increasing second phase volume fraction, however this is done at the cost of decreasing transformation enthalpy and overall FOM.

In Fig. 3.7, FOM is plotted against OTR for the NiTiCu SMAs studied here, with data from traditional polymer-based solid-solid PCMs [56-58], composite PCMs [59-62], and NiTi [4] and NiTiHf [64] SMAs included for comparison. The A_f temperature of each material (equivalently, the melting peak endpoint temperature for traditional PCMs) is denoted by marker color. As shown if Fig. 3.7, NiTi and NiTiHf SMAs have FOM values much higher than traditional PCMs. However, these SMAs generally have higher OTRs, limiting their application and giving them lower thermal cycling frequency. The magnified portion of Fig. 3.7 shows that NiTiCu SMAs achieve higher FOM than traditional PCMs while exhibiting OTRs much lower than NiTi and NiTiHf SMAs, with most NiTiCu alloys showing OTRs between 12 and 20°C. Although polymer-based solid-solid PCMs show similarly low OTRs, they have extremely low FOM values ranging from 3 to 26 $10^6 \cdot J^2/K \cdot s \cdot m^4$ compared to NiTiCu SMAs which range between FOM values of 250 and 1050 $10^6 \cdot J^2/K \cdot s \cdot m^4$. This unique combination of high FOM and low OTR in NiTiCu alloys makes them excellent candidates for thermal energy storage and management applications

where high heat-flux, fast thermal cycling, and/or a narrow operation temperature window are required.

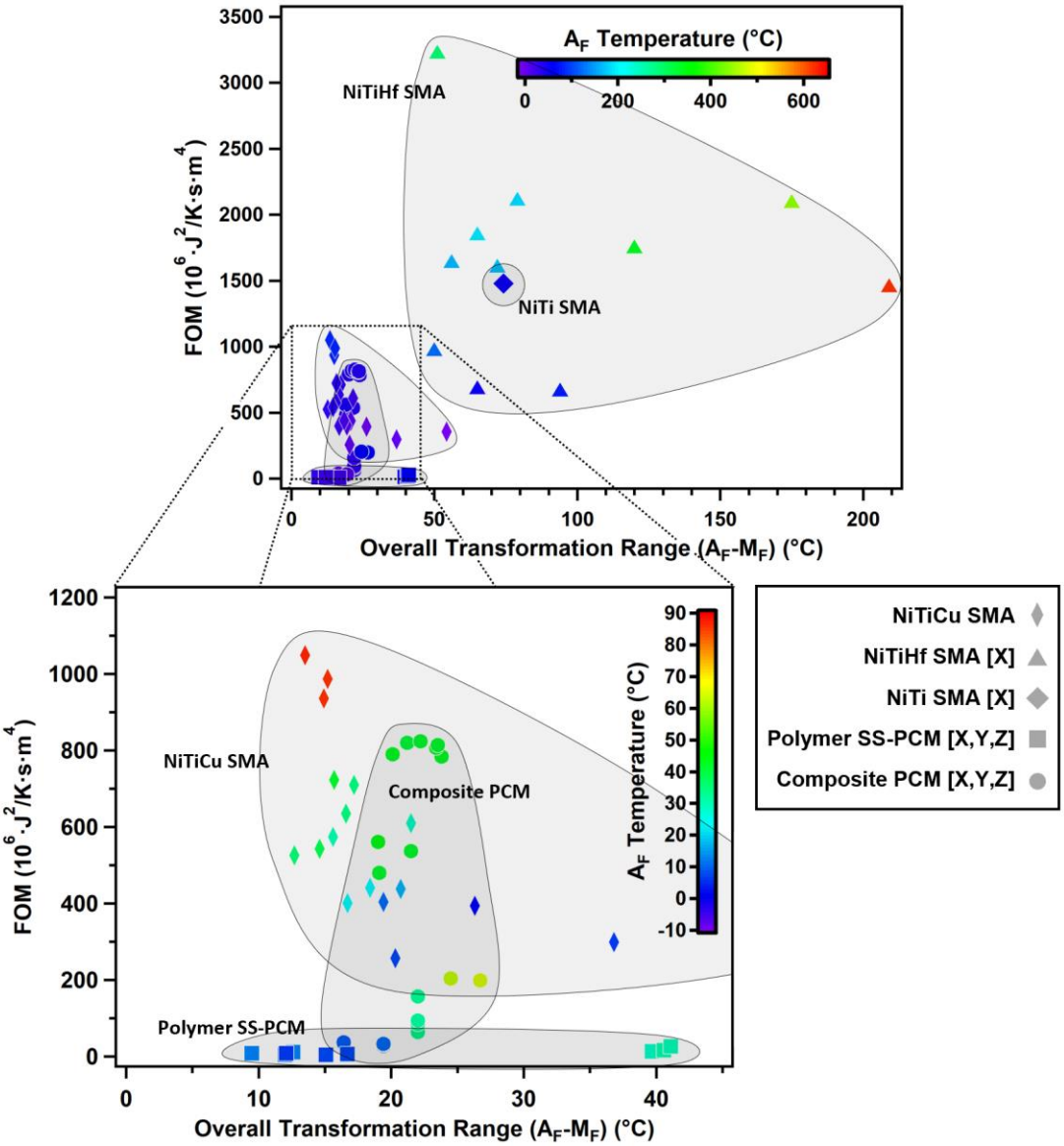

Fig. 3.7. FOM is plotted against OTR for NiTiCu alloys of varying composition with polymer-based solid-solid PCMs [56-58], composite PCMs [59-62], NiTiHf SMAs [64], and NiTi SMA [4] for comparison. Material categories are represented by marker shape, and the A_f temperature (melting peak endpoint temperature for traditional PCMs) of each

material is represented by marker color. The lower window shows a magnified view of the area inside the dotted outline on the upper window.

3.3. Summary and Conclusions

A promising region of the NiTiCu system with narrow OTR was explored to identify candidate alloys for thermal energy storage and management, and the transformation characteristics and thermophysical properties of the alloys therein were examined. The NiTiCu alloys studied here present many characteristics which make them attractive candidates for use as PCMs for thermal energy storage and management applications. Their unique combination of high FOM ranging from 272 to 1049 $10^6 \cdot J^2/K \cdot s \cdot m^4$, and small OTR with most alloys ranging between 12 and 20°C, indicates that they have excellent performance in high-power TES and management applications and the ability to undergo frequent thermal cycling within narrow temperature ranges. Additionally, the alloys exhibit promising cyclic stability, showing only 0.06°C shift in the transformation peak and 0.4-0.7% degradation in transformation enthalpy after 20 thermal cycles. The trends in transformation temperature with respect to composition allow for tuning of NiTiCu alloys for specific TES applications through composition control, with A_f temperatures ranging from -8.1 to 88.7°C. Furthermore, the differences in material properties between the primary and second phases present an opportunity to tailor the properties of the material (e.g. thermal conductivity) to desired levels by adjusting the ratio of the two phases. Thus, SMAs are further established as potential high

performance PCMs, with NiTiCu SMAs providing unique, tunable TES solutions, having low OTRs while maintaining high FOM values.

3.4. Experimental Methods

The materials with the nominal compositions in Table 3.1 were fabricated using vacuum arc melting (VAC) using high purity raw materials (>99.99%) to create 12 g buttons. The samples were flipped and remelted at high current 5 times to ensure homogeneity. The buttons were then sealed in quartz tubes under high vacuum, homogenized at 925°C for 48h, and air cooled to room temperature. The buttons were then cut via wire electrical discharge machining (wire-EDM) to produce 8 mm diameter x 1 mm thick samples for thermal diffusivity measurement, and 3 mm diameter x 1 mm thick samples were cut for differential scanning calorimetry (DSC) and scanning electron microscopy (SEM). The specimens were polished prior to testing and imaging to remove the possible effects of an EDM recast layer.

A TA Instruments Q2000 differential scanning calorimeter (DSC) was used to determine the stress-free phase transformation temperatures of the arc melted buttons. The material was thermally cycled 3 times at a heating-cooling rate of 10°C/min, with selected compositions cycled 20 times to determine cyclic stability. Stress free transformation temperatures were determined from the DSC peaks using the slope line extension method as described in ASTM F2004-17 [122]. The latent heat of transformation was also calculated from the area under the transformation peaks. The microstructure of the samples was observed using FEI Quanta 600 FE-SEM with a voltage of 15 kV. Oxford

energy dispersive X-ray spectroscopy (EDS) system equipped with X-ray mapping and digital imaging was used to determine the composition of the matrix and the second phase present in the material.

Thermal diffusivity was measured using a TA Instruments DXF 200 high-speed Xenon-pulse delivery source and solid-state PIN detector, with measurements taken at approximately 25°C intervals. Specific heat capacity measurements were extracted from the DSC heat flow data using the sapphire standard method. Finally, thermal conductivity was calculated according to $k(T) = \rho \cdot c_p(T) \cdot \alpha(T)$ where k is temperature dependent thermal conductivity, ρ is density, $c_p(T)$ is temperature dependent specific heat capacity, and α(T) is temperature dependent thermal diffusivity. The density of each alloy was determined by Archimedes' method, using the sample weight in air and submerged in water of a known temperature according to the equation $\rho = \rho_w * \frac{w_a}{w_a - w_s}$ where ρ is the sample density, ρ_w is the density of water, w_a is the weight of the sample in air, and w_s is the apparent weight of the sample while submerged in water.

4. CUZNAL SHAPE MEMORY ALLOYS AS HIGH THERMAL CONDUCTIVITY PHASE CHANGE MATERIALS FOR THERMAL ENERGY STORAGE

4.1. Introduction

Shape memory alloys (SMAs) have recently been shown to have excellent thermal energy storage (TES) performance [4, 64], making them preferable to traditional phase change materials (PCMs) in certain thermal energy storage and management applications. Analogous to the melting and recrystallization process of traditional PCMs, the thermally driven forward and reverse martensitic transformations of SMAs allow them to absorb and release large amounts of heat without undergoing significant temperature changes. SMAs offer several benefits over traditional PCMs, including solid-solid transformations which eliminate the need for liquid containment as is necessary in traditional solid-liquid PCMs, and superior performance in fast transient thermal storage applications as quantified by Lu's PCM figure of merit (FOM = $\rho \cdot L \cdot k$, where ρ is density, L is latent heat of transformation, and k is thermal conductivity) [2]. While traditional PCMs such as organics, polymers, and salt hydrates typically show FOM values between 20 and 400 $10^6 \cdot J^2/K \cdot s \cdot m^4$ [3], NiTi SMAs have been demonstrated to have FOM values as high as 1478 $10^6 \cdot J^2/K \cdot s \cdot m^4$ [4]. NiTiCu SMAs exhibit FOM values as high as 1048 $10^6 \cdot J^2/K \cdot s \cdot m^4$ [123] and have additional characteristics desirable in PCMs including excellent cyclic stability and low overall transformation range (A_f-M_f), allowing for frequent thermal cycling. NiTiHf SMAs, which can operate at temperatures exceeding 500°C [38], have achieved FOM values ranging up to 3217 $10^6 \cdot J^2/K \cdot s \cdot m^4$ [64], providing high-temperature

TES solutions. Despite these promising advancements in the characterization of SMA performance in TES applications, the NiTi-based SMAs suffer from certain drawbacks. For example, the NiTiHf compositions with the highest reported FOM values (2000-3000 $10^6 \cdot J^2/K \cdot s \cdot m^4$) are limited to operation temperatures above 100°C, excluding them from applications with low operation temperatures [64]. Furthermore, although the NiTi-based SMAs show high thermal conductivities (8-18 W/m·K) [4, 64] in comparison to traditional PCMs (<1 W/m·K) [3], they are relatively low in comparison to common heat sink materials such as aluminum and copper (236 and 401 W/m·K, respectively). This low thermal conductivity causes poor performance in thermal management applications where high heat flux steady-state heat dissipation is required, such as in microelectronic thermal management. The thermal conductivity of traditional PCMs has been increased by addition of a conductive dispersed phase such as expanded graphite or carbon nanotubes, however the composite thermal conductivities were limited to below 6 W/m·K [59-62]. In light of this, Cu-based SMAs are attractive candidates for TES applications due to their wide-ranging transformation temperatures and high thermal conductivity, which is reported to range between 30 and 120 W/m·K [124]. Among the Cu-based SMAs, CuZnAl alloys are of particular interest, as a one composition was reported to have a thermal conductivity of 120 W/m·K [124]. However, the thermophysical properties of CuZnAl are scarcely reported in literature and their TES performance has not been evaluated. The current study investigates the thermal energy storage performance of CuZnAl SMAs through measurement and analysis of transformation characteristics and thermophysical properties.

4.2. Experimental Methods

Eleven CuZnAl ingots of varying composition were fabricated, with alloy compositions chosen to achieve a wide range of transformation temperatures between -150 and 100°C. The compositions of the alloys are indicated on the phase diagram [125] in Fig. 4.1. The ingots were made according to the procedure shown in Fig. 4.2. Pure elements in the necessary proportions were sealed inside quartz tubes under Ar atmosphere to reduce oxidation and contamination during melting. Melting within a small, sealed volume such as a quartz tube also reduces Zn evaporation, resulting in lower Zn loss from the melt (a common problem in CuZnAl alloy synthesis [126]) and higher compositional accuracy. The tubes were heated at 1225°C for approximately 15 minutes to ensure the metals melted fully. The tubes were then flipped and lightly shaken 3 times with 5-minute intervening heating intervals in order to stir the molten metal and ensure homogeneity in the finished ingots. The furnace temperature was then reduced to 1000°C (just above the melting temperature of the alloys), and subsequently ramped down to 950°C (just below the melting temperature of the alloys) over approximately 5 minutes to slow the solidification process and mitigate shrinkage porosity formation. The alloys were then allowed to air cool to room temperature before undergoing a homogenization heat treatment at 850°C for 2 hours. The ingots were allowed to air cool to room temperature following heat treatment, as quenching from high temperature often causes vacancy formation in Cu-based SMAs, stabilizing the martensite phase and suppressing transformation [127]. Although step-quenching to intermediate temperatures is often used to tune the microstructures of CuZnAl SMAs [128, 129], the complexity associated

with step-quenching thermal treatment is not desirable for scaling and manufacturing of CuZnAl SMAs, and therefore air cooling was performed in this study. After cooling from heat treatment, the finished ingots were cut into test samples via wire electrical discharge machining. Discs with 3 mm diameter and 1 mm thickness were cut for differential scanning calorimetry (DSC) measurements, and discs with 8 mm diameter and 1 mm thickness were cut for thermal diffusivity measurements, scanning electron microscopy (SEM), and X-ray diffraction (XRD) analysis.

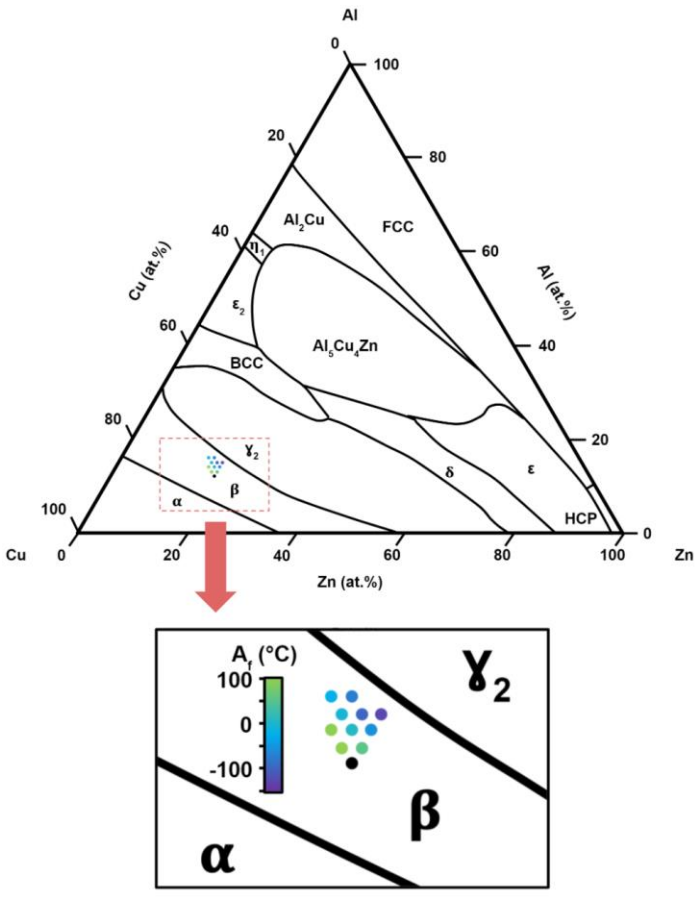

Fig. 4.1. Phase diagram for CuZnAl with the compositions of the fabricated alloys superimposed. The austenite finish temperatures of the alloys are indicated by color. [125]

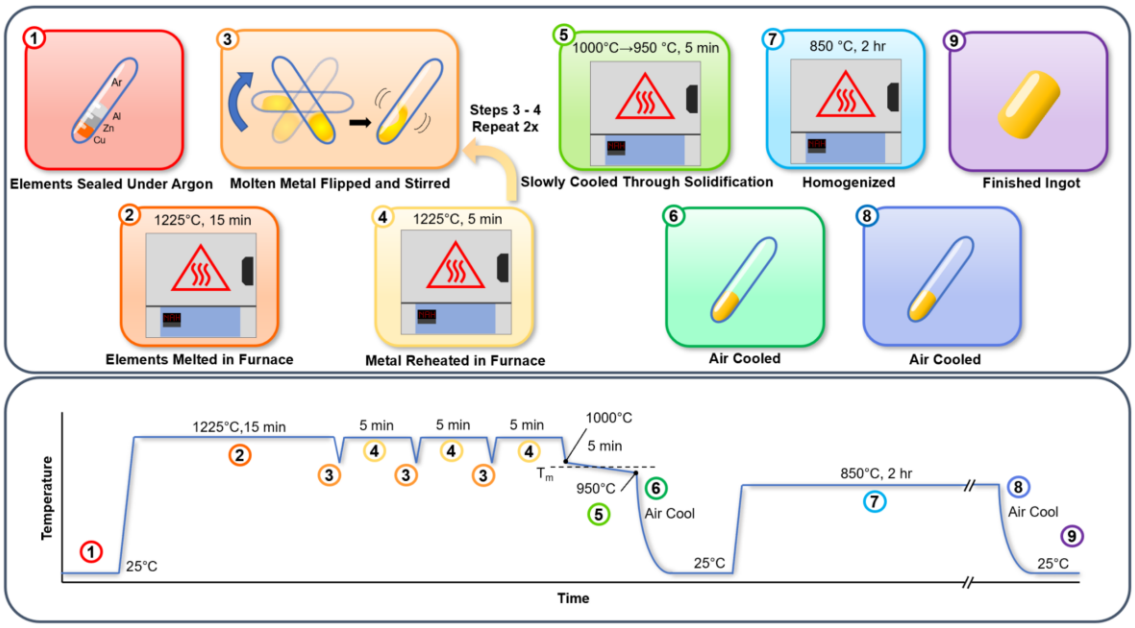

Fig. 4.2. Fabrication steps for the studied alloys are shown in the numbered boxes with corresponding points indicated by the circled numbers on the temperature vs. time plot below.

The microstructures of the samples were imaged using a FEI Quanta 600 FE-SEM, and the matrix compositions were confirmed using an Oxford energy dispersive X-ray spectroscopy (EDS) system with X-ray mapping and digital imaging capability. The phases present in each alloy were determined using X-ray diffraction (XRD).

The transformation temperatures and transformation enthalpies of the alloys were measured using a TA Instruments Q2000 differential scanning calorimeter, heating and cooling the samples between -150 and 200°C at a rate of 10°C/min, in accordance with ASTM standard F2004 [122]. Transformation temperatures were determined by the peak tangent intercept method, and transformation enthalpies were calculated by integrating

heat flow with respect to time under the transformation peak. The cyclic stability of $Cu_{68}Zn_{17}Al_{15}$ was measured over 20 heating cooling cycles between temperature limits of -36 and 18°C (M_f - 20°C and A_f + 20°C, respectively) with a heating/cooling rate of 10°C/min. The specific heat capacities of the samples were determined from the DSC data using the sapphire standard method according to ASTM standard E1269 – 11 [130].

The thermal diffusivity values of selected alloys were measured using a TA Instruments DXF 200 high-speed Xenon-pulse delivery source and solid-state PIN detector. Measurements were taken at approximately 25°C intervals during heating and cooling, with the test temperature ranges chosen to include the high and low temperature phases. The thermal conductivities of the alloys were calculated as a function of temperature according to the equation $k(T) = \alpha(T) \cdot c_p(T) \cdot \rho$, where k(T) is thermal conductivity as a function of temperature, α(T) is thermal diffusivity as a function of temperature, $c_p(T)$ is specific heat capacity as a function of temperature, and ρ is density. The densities of the alloys were measured using Archimedes' method, whereby samples were weighed in air and while submerged in water of a known temperature. The alloy density was calculated as $\rho = \rho_w \cdot \frac{w_a}{w_a - w_s}$, where ρ is the sample density, ρ_w is the density of water at the measurement temperature, w_a is the weight of the sample in air, and w_s is the apparent weight of the sample while submerged in water.

4.3. Results and Discussion

The microstructures of all 11 CuZnAl compositions can be visualized using the 5 representative microstructure images in Fig. 4.3. Depicted are backscatter electron images of fully martensitic microstructures (Fig. 4.3(a)), sparse α_1 bainite separated by martensitic domains with α-phase precipitates (Fig. 4.3(b)), densely clustered α_1 bainite and α-phase precipitates (Fig. 4.3(c)), partially martensitic structure (Fig. 4.3(d)), and fully austenitic structures (Fig. 4.3(e)). A higher magnification SEM image of $Cu_{69}Zn_{18}Al_{13}$ shows 18R martensitic variants forming in between α_1 bainite and α-phase precipitates (Fig. 4.3(f)). The alloy area spectrum matrix compositions confirmed by EDS are listed in Table 3.1, with the references listed to the representative SEM image label from Fig. 4.3(a-e). The phases at room temperature were also confirmed in x-ray diffraction, revealing the presence of ɣ-type precipitates. The high heat treatment temperature of 850°C followed by air cooling allowed the CuZnAl compositions to form precipitates when slowly cooling through lower temperature regimes. It has been shown that temperatures from 200 – 600°C causes rod-like α-phase precipitates to form along grain boundaries and the formation of more α-phase for longer aging times [131].

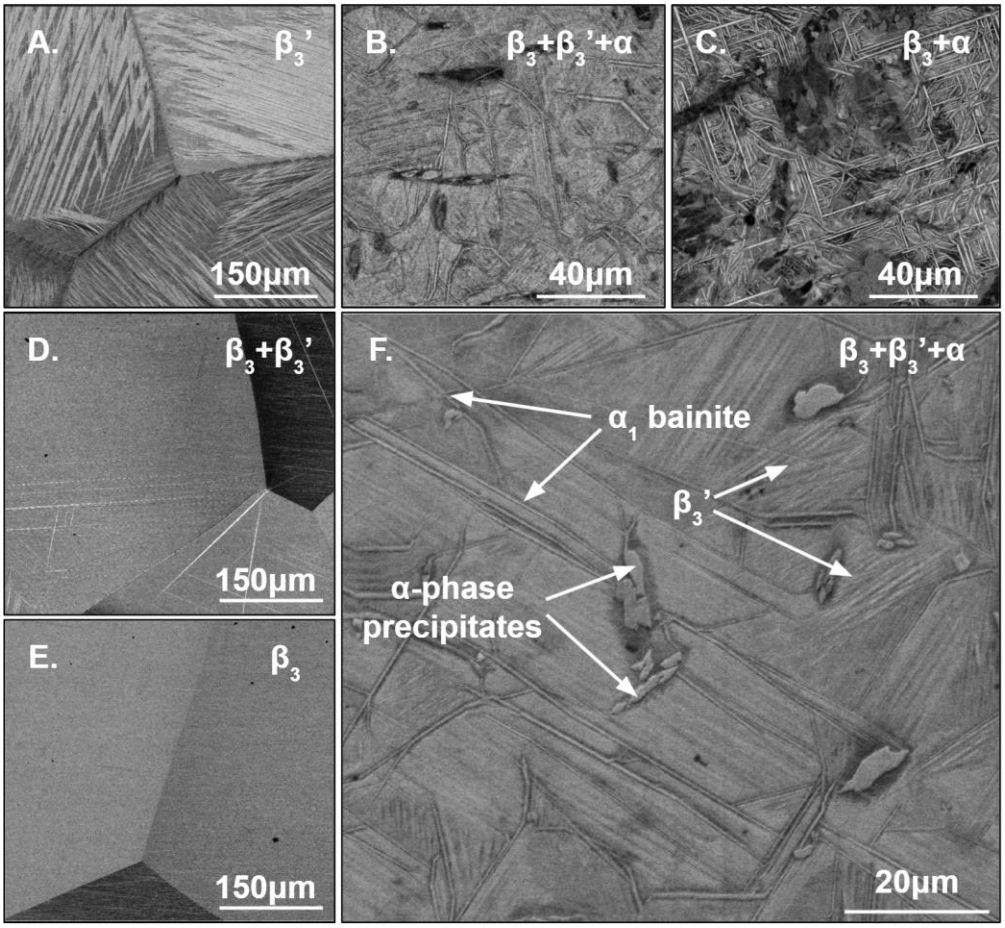

Fig. 4.3. SEM back scatter electron micrographs of the 5 characteristic microstructures observed in the 11 CuZnAl alloys.

Table 4.1. Compositions, transformation temperatures, overall transformation ranges, and transformation enthalpies for the CuZnAl alloys fabricated. Transformation was not detected within the DSC testing temperature range for $Cu_{69}Zn_{19}Al_{12}$. The Zn and Al contents are listed, and Cu content makes up the remaining balance. Nominal compositions are listed first, with measured compositions as determined by EDS shown in parentheses.

Composition: Nominal (measured)		Transformation Temperatures				OTR	Transformation Enthalpies		Microstructure (at 23°C)
Zn (at.%)	Al (at.%)	M_f (°C)	M_s (°C)	A_s (°C)	A_f (°C)	A_f-M_f (°C)	ΔH M→A (J/g)	ΔH A→M (J/g)	Label
16 (16.0)	16 (16.1)	-32	-24.4	-23.8	-19.7	12.3	6.2	5.8	E
17 (16.8)	16 (15.9)	-87.7	-80.4	-82.2	-73.7	14	5	4.6	E
17 (17.1)	15 (14.8)	-15.8	-8.7	-8.5	-2.4	13.4	6.4	6.2	E
18 (18.2)	15 (15.4)	-130.4	-106.6	-120.2	-96.8	33.6	3.3	2.5	E
19 (19.0)	15 (15.1)	-142.4	-135.1	-133.2	-126.3	16.1	3.3	2.5	E
17 (17.3)	14 (14.0)	25.6	71.6	63.2	99.2	73.6	5.8	7.8	A
18 (18.0)	14 (14.2)	-25.9	-5.8	-6.8	8.6	34.5	4.7	4.5	D
19 (18.9)	14 (14.0)	-87.9	-64.1	-74.4	-54.9	33	4.6	4.3	E
18 (18.2)	13 (13.2)	28.5	72.1	67.5	101.8	73.3	3.2	2.4	B
19 (19.1)	13 (13.2)	26.6	35.6	46	55.4	28.8	5.3	6.9	A
19 (18.9)	12 (12.2)	-	-	-	-	-	-	-	C

The A_f and M_f transformation temperatures of the alloys are listed in Table 4.1 and plotted as a function of composition in Fig. 4.4(a). A_f temperatures ranged from -126.3 to 101.8°C, and both A_f and M_f temperatures decreased with increasing Al content and with increasing Zn content, showing good agreement with literature on β to 18R transformations in CuZnAl SMAs [132]. The martensite to austenite transformation enthalpies of the alloys are listed in Table 4.1 and plotted as a function of composition in Fig. 4.4(b). In general, the transformation enthalpies increase with decreasing Zn content

for a given Al content, however $Cu_{69}Zn_{18}Al_{13}$ is an exception to the trend, showing unexpectedly low transformation enthalpy. This low enthalpy is attributed to suppression of martensitic transformation caused by the presence of bainite and α-phase precipitates as shown in Fig. 4.3(b) and 4.3(f). The microstructure of $Cu_{69}Zn_{19}Al_{12}$ was even more densely populated with bainite and α-phase precipitates as shown in Fig. 4.3(c), and as a result, martensitic transformation was fully suppressed, and no transformation was detected by DSC.

$Cu_{68}Zn_{17}Al_{15}$ was selected for cyclic stability characterization because it shows the highest martensite to austenite transformation enthalpy, making it a promising high-FOM candidate. As shown in Fig. 4.5(a), A_f and M_s temperatures shifted only 0.07 and 0.5°C respectively after 20 heating-cooling cycles, showing good stability. M_f temperature showed the greatest shift of -1.8°C, however the diminishing magnitude of the regression line slope indicates that the M_f temperature began to stabilize at higher cycle number. A_s temperature shifted by -1.7°C after 20 cycles, however it did not show the same degree of stabilization as M_f temperature and may therefore continue to shift significantly when tested beyond 20 cycles. The transformation enthalpies are plotted as a function of cycle number in Fig. 4.5(b). The austenite to martensite transformation enthalpy showed a decrease of 5.7% over 20 cycles, however the martensite to austenite transformation enthalpy, which is used in calculation of the FOM, decreased by only 2.6%. The OTR increased by 1.9°C after 20 cycles as shown in Fig. 4.5(c), however it began to stabilize at higher cycle number. The heat flow measured by DSC during the 20 heating-cooling cycles is shown in Fig. 4.5(d).

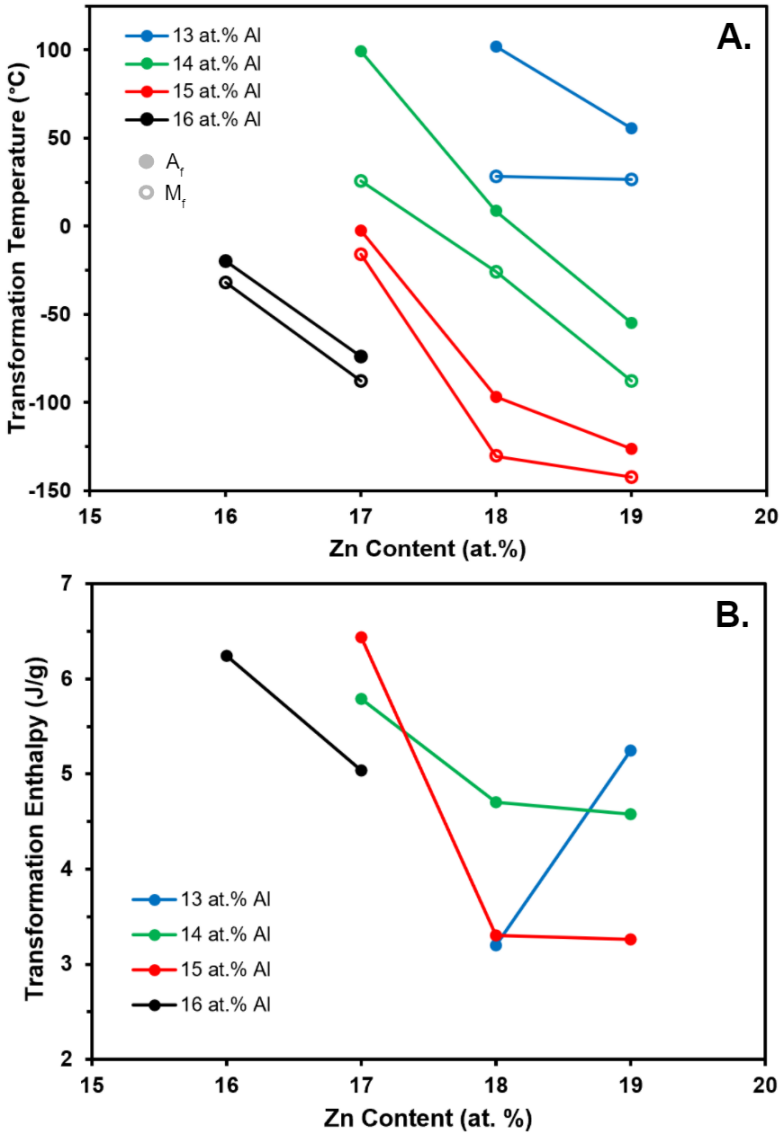

Fig. 4.4. (a) Austenite finish (filled markers) and martensite finish (empty markers) temperatures of CuZnAl alloys plotted against Zn content. Al content is denoted by color. (b) Transformation enthalpies plotted against Zn content with Al content denoted by color.

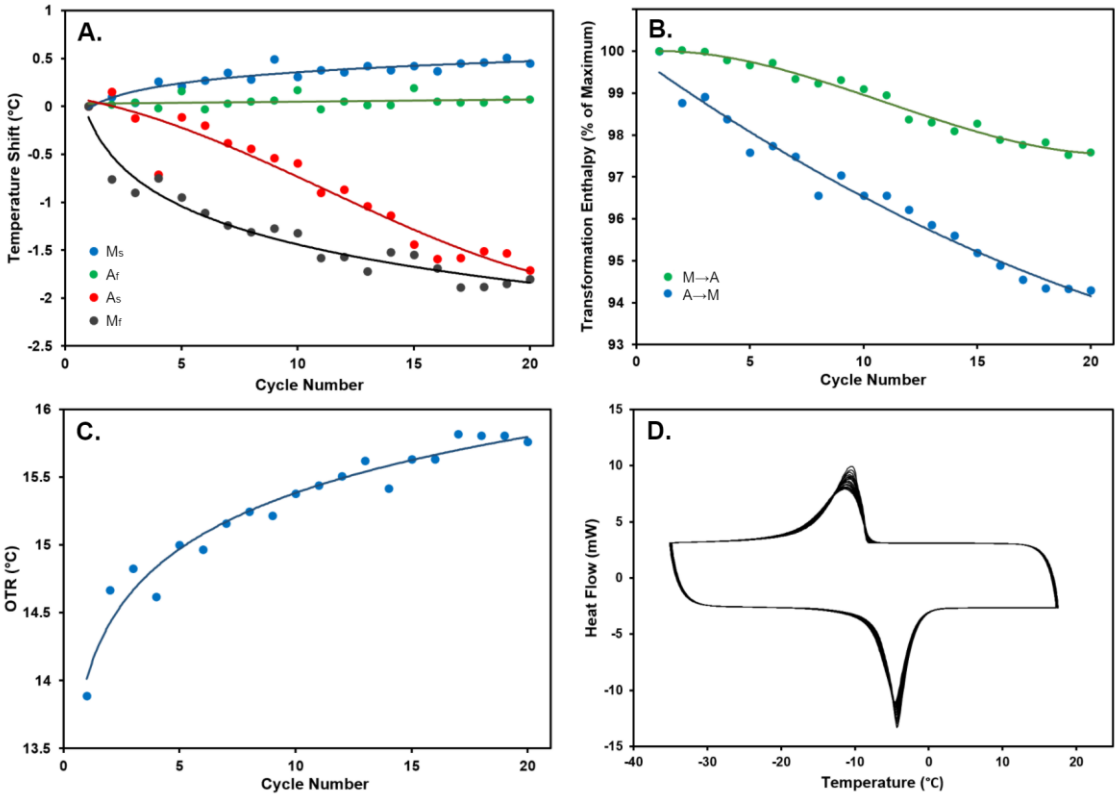

Fig. 4.5. The cyclic stability results from $Cu_{68}Zn_{17}Al_{15}$ measured throughout 20 heating-cooling cycles. Plotted are (a) shifts in transformation temperatures as a function of cycle number, (b) DSC curves from 20 cycles, (c) transformation enthalpies as a percentage of the first-cycle values plotted against cycle number, and (d) overall transformation range (A_f-M_f) as a function of cycle number.

The densities of the alloys, which ranged between 7488 and 7750 kg/m^3, are listed in Table 4.2 and plotted as a function of Al content in Fig. 4.6. Density decreased with increasing Al content as expected due to the low density of Al (2700 kg/m^3) compared to Cu (8960 kg/m^3) and Zn (7130 kg/m^3). No correlation between density and Zn content

was detected because of the small range of compositions explored and the similarity between the densities of Zn and Cu.

The measured thermal conductivities of 6 CuZnAl alloys are listed in Table 4.2. Thermal conductivities, measured at approximately 25°C above A_f temperature, ranged between 59 and 75 W/m·K, however no correlation was found with respect to composition. $Cu_{69}Zn_{19}Al_{12}$ demonstrated the lowest thermal conductivity at 59 W/m·K, which may be attributed to phonon scattering at phase boundaries between the precipitates, bainite, and matrix phases. The measured thermal conductivities are significantly lower than the 120 W/m·K reported in literature [124]. This may be due to compositional or processing differences, especially since CuZnAl alloys show martensitic transformations in a wide range of compositions [124, 132], and commonly undergo widely varying thermal treatments. In the remaining 5 samples for which no thermal conductivity is reported, thermal conductivity could not be accurately measured due to a small amount of shrinkage porosity formed upon solidification of the alloys during fabrication. The specific heat capacities of the alloys (listed in Table 4.2), which were measured in order to calculate thermal conductivity, ranged between 0.391 and 0.529 J/g·K, showing similar, though slightly higher values compared to those reported in literature [124, 133, 134].

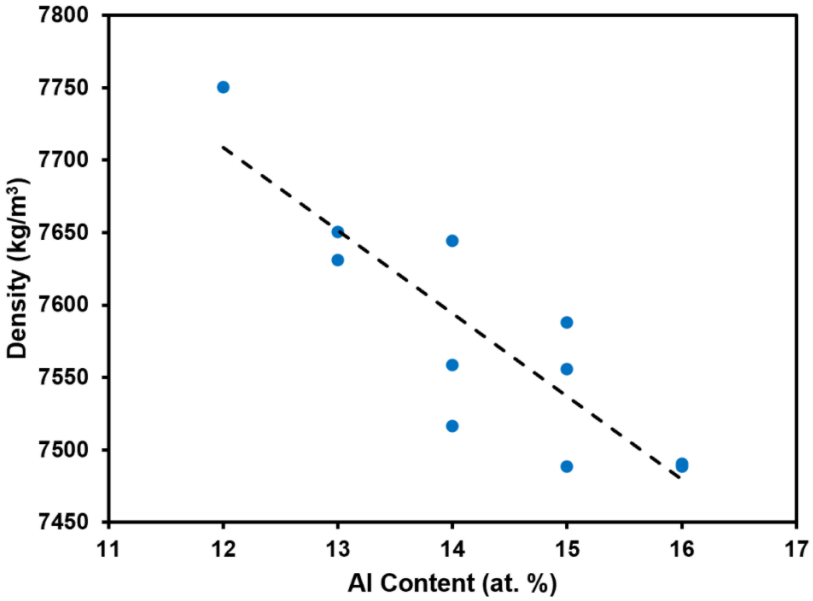

Fig. 4.6. The densities of CuZnAl alloys plotted as a function of Al content (blue markers) with a linear regression indicated by the dashed line.

Table 4.2. Thermophysical properties and FOM values of CuZnAl alloys.

Zn (at.%)	Al (at.%)	Specific Heat Capacity (J/g·K)	ΔH M→A (J/g)	Thermal Conductivity (W/m·K)	Density (kg/m^3)	FOM ($10^6 \cdot J^2/K \cdot s \cdot m^4$)
16	16	0.5	5.8	74.1	7491	3463
17	16	0.529	4.6	74.7	7488	2823
17	15	0.452	6.2	67.4	7588	3313
18	15	-	2.5	-	7488	1717*
19	15	0.455	2.5	65.8	7556	1631
17	14	0.391	7.8	-	7644	3076*
18	14	-	4.5	-	7517	2455*
19	14	-	4.3	-	7559	2406*
18	13	0.405	2.4	-	7631	1697*
19	13	0.51	6.9	75	7651	3012
19	12	0.411	NT	59	7750	NT

*FOM values calculated using an estimated thermal conductivity value of 69.5 W/m·K based on the average of the measured thermal conductivities.

The FOM values of the 10 transforming CuZnAl alloys were calculated as the product of the measured density, thermal conductivity, and transformation enthalpy values, and are listed in Table 4.2. For the 5 alloys which could not undergo thermal conductivity measurement, thermal conductivity was assumed to be 69.5 W/m·K (the average value of the 6 thermal conductivity measurements) for the purpose of FOM calculation. As shown in Fig. 4.7(a), the studied CuZnAl alloys provide a wide range of TES solutions with A_f temperatures between -126.3 and 101.8°C and FOM values between 1631 and 3463 $10^6 \cdot J^2/K \cdot s \cdot m^4$. In terms of FOM, all CuZnAl alloys outperformed traditional solid-liquid and solid-solid PCMs (maximum FOM = 476 $10^6 \cdot J^2/K \cdot s \cdot m^4$) [3, 56-59, 135], composite PCMs (maximum FOM = 824 $10^6 \cdot J^2/K \cdot s \cdot m^4$) [59-62], NiTi SMA (FOM = 1478 $10^6 \cdot J^2/K \cdot s \cdot m^4$) [4], and NiTiCu SMAs (maximum FOM = 1048 $10^6 \cdot J^2/K \cdot s \cdot m^4$) [123]. $Cu_{68}Zn_{16}Al_{16}$ and $Cu_{68}Zn_{17}Al_{15}$ outperformed all NiTiHf SMAs (maximum FOM = 3217 $10^6 \cdot J^2/K \cdot s \cdot m^4$) [64] with FOM values of 3463 and 3313 $10^6 \cdot J^2/K \cdot s \cdot m^4$ respectively. In Fig. 4.7(b), FOM values are plotted against OTR. CuZnAl alloys show excellent combinations of material properties, achieving OTRs as low as those measured in NiTiCu (12°C) [123] with FOM values exceeding those of NiTiHf alloys. Only polymer solid-solid PCMs demonstrate lower OTR with one material achieving 9.5°C [57], however the corresponding FOM value is 3 orders of magnitude lower than CuZnAl alloys at only 8 $10^6 \cdot J^2/K \cdot s \cdot m^4$. Although CuZnAl alloys demonstrate equally low OTR to NiTiCu SMAs while achieving much greater FOM values, NiTiCu alloys show superior cyclic stability [123]. Nonetheless, the thermophysical properties of CuZnAl SMAs promise excellent TES performance.

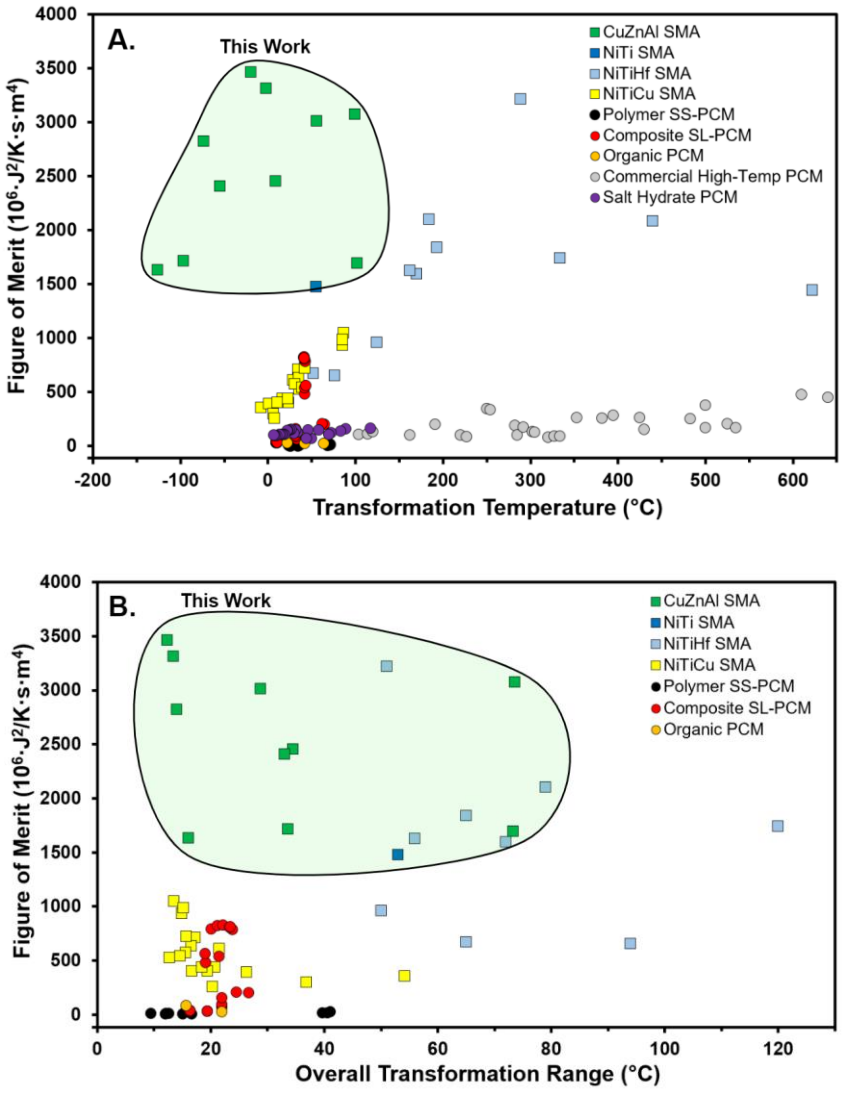

Fig. 4.7. (a) FOM values of CuZnAl alloys plotted against transformation temperature (A_f temperature for SMAs), and (b) FOM values of CuZnAl plotted against overall transformation range with NiTi SMA [4], NiTiHf SMAs [64], NiTiCu SMAs [123], polymer SS-PCMs [56-58], composite PCMs [59-62], organic PCMs [59, 135], commercial high-temperature PCMs [3], and salt hydrate PCMs [3] included for comparison. Due to limitations in data availability, commercial high-temperature PCMs and salt hydrate PCMs were not included in plot (b).

4.4. Summary and Conclusions

The thermophysical properties and transformation characteristics of 11 CuZnAl alloys were analyzed in order to assess the potential TES performance of CuZnAl SMAs. An alloy fabrication procedure was developed, successfully mitigating the difficulty in achieving accurate compositions, reducing porosity, and avoiding the complex step-quenching thermal treatments often associated with CuZnAl alloy synthesis. The transformation temperatures of the alloys showed strong compositional dependence resulting in A_f temperatures ranging between -126.3 and 101.8°C. The observed decrease in transformation temperatures caused by increasing Zn and Al content allow for tuning of CuZnAl SMAs to TES applications with specific operation temperatures. The transformation enthalpies and densities of the alloys also showed trends with respect to composition, assisting in targeting of high FOM values. The high thermal conductivities of the alloys, ranging from 59 to 75 W/m·K, are higher than those of traditional PCMs and NiTi-based SMAs, allowing for high-power TES and steady-state heat dissipation. The FOM values of the alloys, ranging up to 3463 $10^6 \cdot J^2/K \cdot s \cdot m^4$, exceed those of traditional PCMs and NiTi-based SMAs, promising excellent performance in fast transient TES applications. In addition to high FOM, CuZnAl SMAs exhibit OTRs as low as 12°C, making them ideal for TES applications which require frequent thermal cycling or narrow operating temperature ranges. Although further experimentation should be done to fully determine, and if necessary, improve the cyclic stability of CuZnAl SMAs, their excellent thermophysical properties make them attractive PCMs for high-power TES applications.

5. CONCLUSIONS

The thermophysical properties and transformation characteristics of NiTiHf, NiTiCu, and CuZnAl SMAs were measured and analyzed to determine their potential performance as phase change materials for thermal energy storage. Alloys of varying composition from each alloy system were fabricated, and their densities, transformation enthalpies, and thermal conductivities were measured for the purpose of calculating the FOM value of each alloy. The transformation temperatures and overall transformation ranges of the alloys, as well as the cyclic stability of selected alloys, were also characterized. The measured transformation characteristics and thermophysical properties were related to the compositions and microstructures of the alloys, allowing for optimization of TES performance within alloy systems. Based on these experiments and data analysis, the following conclusions were made.

1. SMAs provide several advantages over traditional PCMs, including solid-solid transformations, high thermal conductivity, transformation temperature tunability, and high FOM, making SMAs preferable in high heat flux TES applications.
2. NiTiHf, NiTiCu, and CuZnAl SMAs each present a unique set of thermophysical properties and transformation characteristics, significantly improving upon the TES performance of NiTi SMAs, traditional solid-solid and soli-liquid PCMs, and composite PCMs with enhanced thermal conductivity.

3. The relationships between composition and transformation temperatures are well-mapped in NiTiHf, NiTiCu, and CuZnAl SMAs, allowing for tuning of each alloy system to TES applications with specific operation temperatures through composition control.
4. NiTiHf SMAs achieve more than double the FOM value experimentally determined for NiTi while also providing TES solutions beyond 500°C, greatly exceeding the 100°C temperature limitation of NiTi.
5. The varying FOM values of NiTiHf alloys are predominantly influenced by variations in transformation enthalpy which is strongly influenced by alloy composition. NiTiHf alloys near 20 at.% Hf and 50 at.% Ni show the greatest transformation enthalpies and FOM values.
6. NiTiCu alloys show OTRs as low as 12°C, excellent cyclic stability, and moderately high FOM values, making them excellent for TES applications requiring frequent cycling, narrow operating temperature ranges, and/or a high number of cycles.
7. The densities, transformation enthalpies, and thermal conductivities of NiTiCu SMAs show strong dependence on composition and the amount of second phase present in the material. NiTiCu alloys which are near 50 at.% Ti and have no second phase particles show the highest FOM values and therefore promise the best TES performance within the explored composition space of the NiTiCu system.

8. Zn evaporation during synthesis of CuZnAl alloys can be mitigated by melting the constituent elements within a small, sealed tube, resulting in high compositional accuracy.
9. CuZnAl SMAs exhibit FOM values even higher than those of NiTiHf alloys, while simultaneously achieving OTRs as low as NiTiCu alloys, however the cyclic stability of CuZnAl alloys should be further explored to confirm their viability for TES applications requiring a high number of cycles.
10. The high thermal conductivity (up to 75 W/m·K) of CuZnAl alloys promises superior steady state heat dissipation for thermal management applications compared to NiTi-based SMAs and traditional PCMs.
11. Although NiTiHf and CuZnAl show similarly high FOM values, they achieve them in different ways. As shown in Fig. 5.1, NiTiHf alloys show high FOM mainly due to high volumetric energy storage density, while CuZnAl alloys achieve their high FOM mainly due to high thermal conductivity. These differences in the underlying thermophysical properties make each alloy preferable in different applications depending on specific material property requirements.

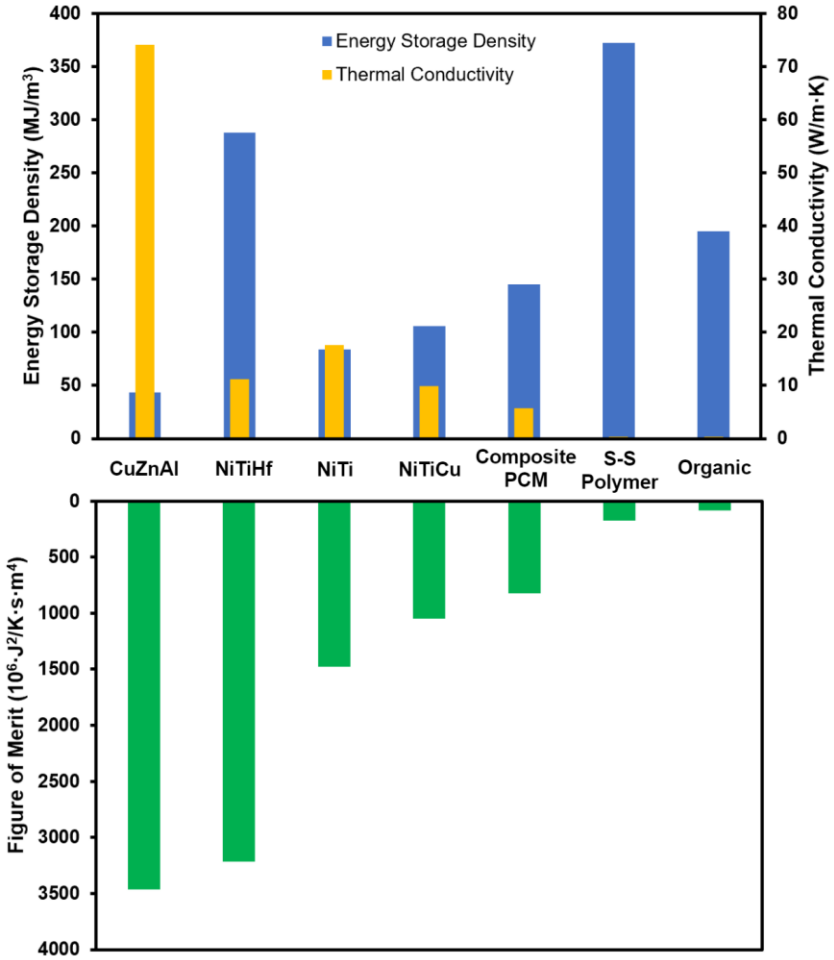

Fig. 5.1. Volumetric energy density, thermal conductivity, and FOM plotted for CuZnAl, NiTiHf, NiTi [4], NiTiCu, composite PCMs [59-62], solid-solid polymer PCMs [56-58], and organic PCMs [59].

6. REFERENCES

[1] M. Irfan Lone and R. Jilte, "A review on phase change materials for different applications," *Materials Today: Proceedings*, 2021/03/02/ 2021, doi: https://doi.org/10.1016/j.matpr.2021.02.050.

[2] T. J. Lu, "Thermal management of high power electronics with phase change cooling," *International Journal of Heat and Mass Transfer*, vol. 43, no. 13, pp. 2245-2256, 2000/07/01/ 2000, doi: https://doi.org/10.1016/S0017-9310(99)00318-X.

[3] P. C. M. P. Limited. "PlusICE Phase Change Materials." https://www.pcmproducts.net/files/PlusICE%20Range-2013.pdf (accessed.

[4] D. J. Sharar, B. F. Donovan, R. J. Warzoha, A. A. Wilson, A. C. Leff, and B. M. Hanrahan, "Solid-state thermal energy storage using reversible martensitic transformations," (in English), *Applied Physics Letters*, vol. 114, no. 14, Apr 8 2019, doi: Artn 14390210.1063/1.5087135.

[5] V. E. Chelnokov and A. Syrkin, "High temperature electronics using SiC: Actual situation and unsolved problems," *Materials Science and Engineering: B*, vol. 46, pp. 248-253, 04/01 1997, doi: 10.1016/S0921-5107(96)01990-3.

[6] Y. Cai, Z. Cheng, Z. Yang, C. W. Tang, K. M. Lau, and K. J. Chen, "High-Temperature Operation of AlGaN/GaN HEMTs Direct-Coupled FET Logic (DCFL) Integrated Circuits," *IEEE Electron Device Letters*, vol. 28, no. 5, pp. 328-331, 2007, doi: 10.1109/LED.2007.895391.

[7] R. S. Pengelly, S. M. Wood, J. W. Milligan, S. T. Sheppard, and W. L. Pribble, "A Review of GaN on SiC High Electron-Mobility Power Transistors and MMICs," *IEEE Transactions on Microwave Theory and Techniques*, vol. 60, no. 6, pp. 1764-1783, 2012, doi: 10.1109/TMTT.2012.2187535.

[8] S. A. Payne *et al.*, "Diode arrays, crystals, and thermal management for solid-state lasers," *IEEE Journal of Selected Topics in Quantum Electronics*, vol. 3, no. 1, pp. 71-81, 1997.

[9] L. Xingsheng, M. H. Hu, C. G. Caneau, R. Bhat, and Z. Chung-En, "Thermal management strategies for high power semiconductor pump lasers," *IEEE Transactions on Components and Packaging Technologies*, vol. 29, no. 2, pp. 268-276, 2006, doi: 10.1109/TCAPT.2006.875878.

[10] D. J. Sharar, A. C. Leff, A. A. Wilson, and A. Smith, "High-capacity high-power thermal energy storage using solid-solid martensitic transformations," *Applied Thermal Engineering*, vol. 187, p. 116490, 2021/03/25/ 2021, doi: https://doi.org/10.1016/j.applthermaleng.2020.116490.

[11] P. J. Shamberger and N. M. Bruno, "Review of metallic phase change materials for high heat flux transient thermal management applications," *Applied Energy*, vol. 258, p. 113955, 2020/01/15/ 2020, doi: https://doi.org/10.1016/j.apenergy.2019.113955.

[12] R. J. Warzoha *et al.*, "Grain growth-induced thermal property enhancement of NiTi shape memory alloys for elastocaloric refrigeration and thermal energy storage systems," *International Journal of Heat and Mass Transfer*, vol. 154, p.

119760, 2020/06/01/ 2020, doi: https://doi.org/10.1016/j.ijheatmasstransfer.2020.119760.

[13] G. Rondelli, "Corrosion resistance tests on NiTi shape memory alloy," *Biomaterials*, vol. 17, no. 20, pp. 2003-2008, 1996/10/01/ 1996, doi: https://doi.org/10.1016/0142-9612(95)00352-5.

[14] T. Hu, C. L. Chu, Y. C. Xin, S. L. Wu, K. W. K. Yeung, and P. K. Chu, "Corrosion products and mechanism on NiTi shape memory alloy in physiological environment," (in English), *J Mater Res*, vol. 25, no. 2, pp. 350-358, Feb 2010, doi: 10.1557/Jmr.2010.0051.

[15] J. Khalil-Allafi, B. Amin-Ahmadi, and M. Zare, "Biocompatibility and corrosion behavior of the shape memory NiTi alloy in the physiological environments simulated with body fluids for medical applications," (in English), *Mat Sci Eng C-Mater*, vol. 30, no. 8, pp. 1112-1117, Oct 12 2010, doi: 10.1016/j.msec.2010.06.007.

[16] E. Hornbogen, "Ausforming of NiTi," (in English), *J Mater Sci*, vol. 34, no. 3, pp. 599-606, Feb 1 1999, doi: Doi 10.1023/A:1004563216567.

[17] B. Kockar, I. Karaman, J. I. Kim, Y. J. Chumlyakov, J. Sharp, and C. J. Yu, "Thermomechanical cyclic response of an ultrafine-grained NiTi shape memory alloy," (in English), *Acta Materialia*, vol. 56, no. 14, pp. 3630-3646, Aug 2008, doi: 10.1016/j.actamat.2008.04.001.

[18] B. Kockar, I. Karaman, A. Kulkarni, Y. Chumlyakov, and I. V. Kireeva, "Effect of severe ausforming via equal channel angular extrusion on the shape memory

response of a NiTi alloy," (in en), *Journal of Nuclear Materials,* vol. 361, no. 2-3, pp. 298-305, 04/2007 2007, doi: 10.1016/j.jnucmat.2006.12.007.

[19] J. van Humbeeck, "Shape memory materials: State of the art and requirements for future applications," (in English), *J Phys Iv,* vol. 7, no. C5, pp. 3-12, Nov 1997, doi: DOI 10.1051/jp4:1997501.

[20] H. Nakayama, K. Tsuchiya, Z. G. Liu, M. Umemoto, K. Morii, and T. Shimizu, "Process of nanocrystallization and partial amorphization by cold rolling in TiNi," (in English), *Mater Trans,* vol. 42, no. 9, pp. 1987-1993, Sep 2001, doi: DOI 10.2320/matertrans.42.1987.

[21] K. Tsuchiya *et al.*, "Production of TiNi amorphous/nanocrystalline wires with high strength and elastic modulus by severe cold drawing," (in English), *Scripta Materialia,* vol. 60, no. 9, pp. 749-752, May 2009, doi: 10.1016/j.scriptamat.2008.12.058.

[22] C. P. Frick *et al.*, "Thermal processing of polycrystalline NiTi shape memory alloys," (in English), *Mat Sci Eng a-Struct,* vol. 405, no. 1-2, pp. 34-49, Sep 25 2005, doi: 10.1016/j.msea.2005.05.102.

[23] D. Treppmann and E. Hornbogen, "On the influence of thermomechanical treatments on shape memory alloys," (in English), *J Phys Iv,* vol. 7, no. C5, pp. 211-220, Nov 1997, doi: DOI 10.1051/jp4:1997533.

[24] V. E. Chelnokov and A. L. Syrkin, "High temperature electronics using SiC: actual situation and unsolved problems," *Materials Science and Engineering: B,*

vol. 46, no. 1, pp. 248-253, 1997/04/01/ 1997, doi: https://doi.org/10.1016/S0921-5107(96)01990-3.

[25] J. Frenzel, A. Wieczorek, I. Opahle, B. Maaß, R. Drautz, and G. Eggeler, "On the effect of alloy composition on martensite start temperatures and latent heats in Ni–Ti-based shape memory alloys," *Acta Materialia*, vol. 90, pp. 213-231, 2015/05/15/ 2015, doi: https://doi.org/10.1016/j.actamat.2015.02.029.

[26] L. Casalena *et al.*, "Mechanical behavior and microstructural analysis of NiTi-40Au shape memory alloys exhibiting work output above 400 C," *Intermetallics*, vol. 86, pp. 33-44, 2017.

[27] A. N. Bucsek, G. A. Hudish, G. S. Bigelow, R. D. Noebe, and A. P. Stebner, "Composition, Compatibility, and the Functional Performances of Ternary NiTiX High-Temperature Shape Memory Alloys," *Shape Memory and Superelasticity*, vol. 2, no. 1, pp. 62-79, 2016/03/01 2016, doi: 10.1007/s40830-016-0052-5.

[28] L. Casalena *et al.*, "Transformation and Deformation Characterization of NiTiHf and NiTiAu High Temperature Shape Memory Alloys," *Microscopy and Microanalysis*, vol. 21, no. S3, pp. 607-608, 2015, doi: 10.1017/S1431927615003839.

[29] J. Ma, I. Karaman, and R. Noebe, "High temperature shape memory alloys," *International Materials Reviews*, vol. 55, pp. 257-315, 09/01 2010, doi: 10.1179/095066010X12646898728363.

[30] A. Evirgen, I. Karaman, R. Santamarta, J. Pons, C. Hayrettin, and R. D. Noebe, "Relationship between crystallographic compatibility and thermal hysteresis in

Ni-rich NiTiHf and NiTiZr high temperature shape memory alloys," *Acta Materialia*, vol. 121, pp. 374-383, 2016/12/01/ 2016, doi: https://doi.org/10.1016/j.actamat.2016.08.065.

[31] O. Karakoc *et al.*, "Role of microstructure on the actuation fatigue performance of Ni-Rich NiTiHf high temperature shape memory alloys," *Acta Materialia*, vol. 175, pp. 107-120, 2019/08/15/ 2019, doi: https://doi.org/10.1016/j.actamat.2019.05.051.

[32] O. Karakoc *et al.*, "Effects of training on the thermomechanical behavior of NiTiHf and NiTiZr high temperature shape memory alloys," *Materials Science and Engineering: A*, vol. 794, p. 139857, 2020/09/09/ 2020, doi: https://doi.org/10.1016/j.msea.2020.139857.

[33] K. C. Atli, B. E. Franco, I. Karaman, D. Gaydosh, and R. D. Noebe, "Influence of crystallographic compatibility on residual strain of TiNi based shape memory alloys during thermo-mechanical cycling," *Materials Science and Engineering: A*, vol. 574, pp. 9-16, 2013/07/01/ 2013, doi: https://doi.org/10.1016/j.msea.2013.02.035.

[34] K. C. Atli, I. Karaman, and R. D. Noebe, "Work output of the two-way shape memory effect in Ti50.5Ni24.5Pd25 high-temperature shape memory alloy," *Scripta Materialia*, vol. 65, no. 10, pp. 903-906, 2011/11/01/ 2011, doi: https://doi.org/10.1016/j.scriptamat.2011.08.006.

[35] B. Kockar *et al.*, "Role of severe plastic deformation on the cyclic reversibility of a Ti50.3Ni33.7Pd16 high temperature shape memory alloy," *Acta Materialia*,

vol. 58, no. 19, pp. 6411-6420, 2010/11/01/ 2010, doi: https://doi.org/10.1016/j.actamat.2010.08.003.

[36] J. Van Humbeeck, "Shape memory alloys: Multi-purpose functional materials," (in English), *Arch Metall Mater*, vol. 49, no. 4, pp. 735-752, 2004. [Online]. Available: <Go to ISI>://WOS:000227653700002.

[37] K. P. Mohanchandra, D. Shin, and G. P. Carman, "Deposition and characterization of Ti-Ni-Pd and Ti-Ni-Pt shape memory alloy thin films," (in English), *Smart Mater Struct*, vol. 14, no. 5, pp. S312-S316, Oct 2005, doi: 10.1088/0964-1726/14/5/021.

[38] T. Umale, D. Salas, B. Tomes, R. Arroyave, and I. Karaman, "The effects of wide range of compositional changes on the martensitic transformation characteristics of NiTiHf shape memory alloys," *Scripta Materialia*, vol. 161, pp. 78-83, 2019/03/01/ 2019, doi: https://doi.org/10.1016/j.scriptamat.2018.10.008.

[39] P. J. Shamberger, "Cooling Capacity Figure of Merit for Phase Change Materials," *Journal of Heat Transfer*, vol. 138, no. 2, 2015, doi: 10.1115/1.4031252.

[40] L. Shao *et al.*, "Figure-of-merit for phase-change materials used in thermal management," *International Journal of Heat and Mass Transfer*, vol. 101, pp. 764-771, 2016/10/01/ 2016, doi: https://doi.org/10.1016/j.ijheatmasstransfer.2016.05.040.

[41] O. Benafan, G. S. Bigelow, and D. A. Scheiman, "Transformation behavior in NiTi-20Hf shape memory alloys - Transformation temperatures and hardness,"

(in English), *Scripta Materialia*, vol. 146, pp. 251-254, Mar 15 2018, doi: 10.1016/j.scriptamat.2017.11.050.

[42] *F2004-17 Standard Test Method for Transformation Temperature of Nickel-Titanium Alloys by Thermal Analysis*, A. International, West Conshohocken, PA, 2017 2017.

[43] T. Duerig and A. Pelton, "Ti-Ni shape memory alloys," *Materials properties handbook: titanium alloys*, vol. 1, pp. 1035-1048, 1994.

[44] J. Frenzel, E. P. George, A. Dlouhy, C. Somsen, M. F. X. Wagner, and G. Eggeler, "Influence of Ni on martensitic phase transformations in NiTi shape memory alloys," *Acta Materialia*, vol. 58, no. 9, pp. 3444-3458, 2010/05/01/ 2010, doi: https://doi.org/10.1016/j.actamat.2010.02.019.

[45] A. M. Pérez-Sierra, J. Pons, R. Santamarta, I. Karaman, and R. D. Noebe, "Stability of a Ni-rich Ni-Ti-Zr high temperature shape memory alloy upon low temperature aging and thermal cycling," *Scripta Materialia*, vol. 124, pp. 47-50, 11// 2016, doi: https://doi.org/10.1016/j.scriptamat.2016.06.029.

[46] R. Santamarta *et al.*, "Effect of Thermal Treatments on Ni-Mn-Ga and Ni-Rich Ni-Ti-Hf/Zr High-Temperature Shape Memory Alloys," (in English), *Shape Memory and Superelasticity*, vol. 1, no. 4, pp. 418-428, Dec 2015, doi: 10.1007/s40830-015-0043-y.

[47] H. Karaca, E. Açar, H. Tobe, and S. Saghaian, "NiTiHf-based shape memory alloys," *Materials Science and Technology*, vol. 30, pp. 1530-1544, 11/01 2014, doi: 10.1179/1743284714Y.0000000598.

[48] N. Babacan, M. Bilal, C. Hayrettin, J. Liu, O. Benafan, and I. Karaman, "Effects of cold and warm rolling on the shape memory response of Ni50Ti30Hf20 high-temperature shape memory alloy," (in English), *Acta Materialia*, vol. 157, pp. 228-244, Sep 15 2018, doi: 10.1016/j.actamat.2018.07.009.

[49] H. Berman, E. West, and A. Rozner, "Anomalous heat capacity of TiNi," *Journal of Applied Physics*, vol. 38, no. 11, pp. 4473-4476, 1967.

[50] F. Cheng, L. Hu, J. N. Reddy, I. Karaman, E. Hoffman, and M. Radovic, "Temperature-dependent thermal properties of a shape memory alloy/MAX phase composite: Experiments and modeling," *Acta Materialia*, vol. 68, pp. 267-278, 2014/04/15/ 2014, doi: https://doi.org/10.1016/j.actamat.2013.12.014.

[51] B. Ingale, W. Wei, P. Chang, Y. Kuo, and S.-K. Wu, "Anomalous transport and thermal properties of NiTi and with Cu and Fe-doped shape memory alloys near the martensitic transition," *Journal of Applied Physics*, vol. 110, p. 113721, 2011.

[52] B. Ramachandran, R. Tang, P. C. Chang, Y. Kuo, C. Chien, and S.-K. Wu, "Cu-substitution effect on thermoelectric properties of the TiNi-based shape memory alloys," *Journal of Applied Physics*, vol. 113, p. 203702, 2013.

[53] "Phase Change Material Products Limited - PlusICE Phase Change Materials." https://www.pcmproducts.net/files/PlusICE%20Range-2013.pdf (accessed.

[54] W. Li *et al.*, "Study of solid–solid phase change of (n-CnH2n+1NH3)2MCl4 for thermal energy storage," *Thermochimica Acta*, vol. 326, no. 1, pp. 183-186, 1999/02/08/ 1999, doi: https://doi.org/10.1016/S0040-6031(98)00497-3.

[55] A. Fallahi, G. Guldentops, M. Tao, S. Granados-Focil, and S. Van Dessel, "Review on solid-solid phase change materials for thermal energy storage: Molecular structure and thermal properties," *Applied Thermal Engineering*, vol. 127, pp. 1427-1441, 09/01 2017, doi: 10.1016/j.applthermaleng.2017.08.161.

[56] A. Sarı, C. Alkan, A. Biçer, and A. Karaipekli, "Synthesis and thermal energy storage characteristics of polystyrene-graft-palmitic acid copolymers as solid–solid phase change materials," *Solar Energy Materials and Solar Cells*, vol. 95, no. 12, pp. 3195-3201, 2011/12/01/ 2011, doi: https://doi.org/10.1016/j.solmat.2011.07.003.

[57] A. Sarı, C. Alkan, and Ö. Lafçı, "Synthesis and thermal properties of poly(styrene-co-ally alcohol)-graft-stearic acid copolymers as novel solid–solid PCMs for thermal energy storage," *Solar Energy*, vol. 86, no. 9, pp. 2282-2292, 2012/09/01/ 2012, doi: https://doi.org/10.1016/j.solener.2012.04.018.

[58] A. Sarı, C. Alkan, and A. Biçer, "Synthesis and thermal properties of polystyrene-graft-PEG copolymers as new kinds of solid–solid phase change materials for thermal energy storage," *Materials Chemistry and Physics*, vol. 133, no. 1, pp. 87-94, 2012/03/15/ 2012, doi: https://doi.org/10.1016/j.matchemphys.2011.12.056.

[59] J.-L. Zeng *et al.*, "Tetradecanol/expanded graphite composite form-stable phase change material for thermal energy storage," *Solar Energy Materials and Solar Cells*, vol. 127, pp. 122-128, 2014/08/01/ 2014, doi: https://doi.org/10.1016/j.solmat.2014.04.015.

[60] B. Wu, D. Lao, R. Fu, X. Su, H. Liu, and X. Jin, "Novel PEG/EP form-stable phase change materials with high thermal conductivity enhanced by 3D ceramics network," *Ceramics International*, vol. 46, no. 16, Part A, pp. 25285-25292, 2020/11/01/ 2020, doi: https://doi.org/10.1016/j.ceramint.2020.06.321.

[61] X. Wu *et al.*, "Experimental Study of the Thermal Properties of a Homogeneous Dispersion System of a Paraffin-based Composite Phase Change Materials," *Journal of Energy Storage*, vol. 36, p. 102398, 2021/04/01/ 2021, doi: https://doi.org/10.1016/j.est.2021.102398.

[62] M. Li, "A nano-graphite/paraffin phase change material with high thermal conductivity," *Applied Energy*, vol. 106, pp. 25-30, 2013/06/01/ 2013, doi: https://doi.org/10.1016/j.apenergy.2013.01.031.

[63] J. Khalil-Allafi and B. Amin-Ahmadi, "The effect of chemical composition on enthalpy and entropy changes of martensitic transformations in binary NiTi shape memory alloys," *Journal of Alloys and Compounds*, vol. 487, no. 1, pp. 363-366, 2009/11/13/ 2009, doi: https://doi.org/10.1016/j.jallcom.2009.07.135.

[64] N. Hite *et al.*, "NiTiHf shape memory alloys as phase change thermal storage materials," *Acta Materialia*, vol. 218, p. 117175, 2021/10/01/ 2021, doi: https://doi.org/10.1016/j.actamat.2021.117175.

[65] J. Frenzel, E. P. George, A. Dlouhy, C. Somsen, M.-X. Wagner, and G. Eggeler, "Influence of Ni on martensitic phase transformations in NiTi shape memory alloys," *Acta Materialia*, vol. 58, no. 9, pp. 3444-3458, 2010.

[66] Z. Wang, X. Zu, S. Zhu, and L. Wang, "Temperature memory effect induced by incomplete transformation in TiNi shape memory alloy," *Materials Letters*, vol. 59, no. 4, pp. 491-494, 2005.

[67] Y. Liu, J. Laeng, T. Chin, and T.-H. Nam, "Effect of incomplete thermal cycling on the transformation behaviour of NiTi," *Materials Science and Engineering: A*, vol. 435, pp. 251-257, 2006.

[68] R. F. Hamilton, H. Sehitoglu, Y. Chumlyakov, and H. J. Maier, "Stress dependence of the hysteresis in single crystal NiTi alloys," *Acta Materialia*, vol. 52, no. 11, pp. 3383-3402, 2004/06/21/ 2004, doi: https://doi.org/10.1016/j.actamat.2004.03.038.

[69] Z. Zhang, R. D. James, and S. Müller, "Energy barriers and hysteresis in martensitic phase transformations," *Acta Materialia*, vol. 57, no. 15, pp. 4332-4352, 2009.

[70] J. M. Ball, C. Chu, and R. D. James, "Hysteresis during stress-induced variant rearrangement," *Le Journal de Physique IV*, vol. 5, no. C8, pp. C8-245-C8-251, 1995.

[71] K. Atli, B. Franco, I. Karaman, D. Gaydosh, and R. Noebe, "Influence of crystallographic compatibility on residual strain of TiNi based shape memory alloys during thermo-mechanical cycling," *Materials Science and Engineering: A*, vol. 574, pp. 9-16, 2013.

[72] P. Potapov, A. Shelyakov, A. Gulyaev, E. Svistunov, N. Matveeva, and D. Hodgson, "Effect of Hf on the structure of Ni-Ti martensitic alloys," *Materials Letters*, vol. 32, no. 4, pp. 247-250, 1997.

[73] A. Evirgen, I. Karaman, R. Santamarta, J. Pons, C. Hayrettin, and R. Noebe, "Relationship between crystallographic compatibility and thermal hysteresis in Ni-rich NiTiHf and NiTiZr high temperature shape memory alloys," *Acta Materialia*, vol. 121, pp. 374-383, 2016.

[74] J. Cui *et al.*, "Combinatorial search of thermoelastic shape-memory alloys with extremely small hysteresis width," *Nature materials*, vol. 5, no. 4, pp. 286-290, 2006.

[75] A. Evirgen, F. Basner, I. Karaman, R. D. Noebe, J. Pons, and R. Santamarta, "Effect of aging on the martensitic transformation characteristics of a Ni-rich NiTiHf high temperature shape memory alloy," *Functional Materials Letters*, vol. 5, no. 04, p. 1250038, 2012.

[76] R. D. James and K. F. Hane, "Martensitic transformations and shape-memory materials," *Acta materialia*, vol. 48, no. 1, pp. 197-222, 2000.

[77] M. Zarinejad and Y. Liu, "Dependence of Transformation Temperatures of NiTi-based Shape-Memory Alloys on the Number and Concentration of Valence Electrons," *Advanced Functional Materials*, vol. 18, no. 18, pp. 2789-2794, 2008.

[78] A. Nespoli, E. Villa, and S. Besseghini, "Characterization of the martensitic transformation in Ni50− xTi50Cux alloys through pure thermal measurements," *Journal of alloys and compounds*, vol. 509, no. 3, pp. 644-647, 2011.

[79] Z. Zhang, J. Frenzel, K. Neuking, and G. Eggeler, "Vacuum induction melting of ternary NiTiX (X= Cu, Fe, Hf, Zr) shape memory alloys using graphite crucibles," *Materials transactions*, vol. 47, no. 3, pp. 661-669, 2006.

[80] R. Zarnetta, P. J. S. Buenconsejo, A. Savan, S. Thienhaus, and A. Ludwig, "High-throughput study of martensitic transformations in the complete Ti–Ni–Cu system," *Intermetallics*, vol. 26, pp. 98-109, 2012/07/01/ 2012, doi: https://doi.org/10.1016/j.intermet.2012.03.044.

[81] Y. Hattori, T. Taguchi, H. Y. Kim, and S. Miyazaki, "Effect of stoichiometry on shape memory properties and functional stability of Ti–Ni–Pd alloys," *Materials*, vol. 12, no. 5, p. 798, 2019.

[82] K. Atli, I. Karaman, and R. Noebe, "Work output of the two-way shape memory effect in Ti50. 5Ni24. 5Pd25 high-temperature shape memory alloy," *Scripta Materialia*, vol. 65, no. 10, pp. 903-906, 2011.

[83] T. H. Nam, T. Saburi, and K. i. Shimizu, "Cu-content dependence of shape memory characteristics in Ti–Ni–Cu alloys," *Materials Transactions, JIM*, vol. 31, no. 11, pp. 959-967, 1990.

[84] H. Li, K. Qiu, F. Zhou, L. Li, and Y. Zheng, "Design and development of novel antibacterial Ti-Ni-Cu shape memory alloys for biomedical application," *Scientific reports*, vol. 6, no. 1, pp. 1-11, 2016.

[85] S.-H. Chang and S.-H. Hsiao, "Inherent internal friction of Ti50Ni50− xCux shape memory alloys measured under isothermal conditions," *Journal of alloys and compounds,* vol. 586, pp. 69-73, 2014.

[86] T. H. Nam, T. Saburi, and K. i. Shimizu, "Effect of thermo-mechanical treatment on shape memory characteristics in a Ti-40Ni-10Cu (at%) alloy," *Materials Transactions, JIM,* vol. 32, no. 9, pp. 814-820, 1991.

[87] K. Lin and S. Wu, "Annealing effect on martensitic transformation of severely cold-rolled Ti50Ni40Cu10 shape memory alloy," *Scripta materialia,* vol. 56, no. 7, pp. 589-592, 2007.

[88] O. W. Bertacchini, D. C. Lagoudas, and E. Patoor, "Thermomechanical transformation fatigue of tinicu sma actuators under a corrosive environment–part i: Experimental results," *International Journal of Fatigue,* vol. 31, no. 10, pp. 1571-1578, 2009.

[89] S. Besseghini, E. Villa, and A. Tuissi, "Ni□ Ti□ Hf shape memory alloy: effect of aging and thermal cycling," *Materials Science and Engineering: A,* vol. 273, pp. 390-394, 1999.

[90] K. Chastaing, P. Vermaut, P. Ochin, C. Segui, J. Laval, and R. Portier, "Effect of Cu and Hf additions on NiTi martensitic transformation," *Materials Science and Engineering: A,* vol. 438, pp. 661-665, 2006.

[91] D. H. Dai Hsu *et al.*, "The effect of aluminum additions on the thermal, microstructural, and mechanical behavior of NiTiHf shape memory alloys," *Journal of Alloys and Compounds,* vol. 638, pp. 67-76, 2015.

[92] G. S. Ded, "Characterization of Ni-rich NiTiHf based high temperature shape memory alloys," 2010.

[93] A. Evirgen, I. Karaman, R. Santamarta, J. Pons, and R. Noebe, "Microstructural characterization and shape memory characteristics of the Ni50. 3Ti34. 7Hf15 shape memory alloy," *Acta Materialia,* vol. 83, pp. 48-60, 2015.

[94] A. Evirgen, I. Karaman, R. Noebe, R. Santamarta, and J. Pons, "Effect of precipitation on the microstructure and the shape memory response of the Ni50. 3Ti29. 7Zr20 high temperature shape memory alloy," *Scripta Materialia,* vol. 69, no. 5, pp. 354-357, 2013.

[95] A. Evirgen, I. Karaman, J. Pons, R. Santamarta, and R. Noebe, "Role of nano-precipitation on the microstructure and shape memory characteristics of a new Ni50. 3Ti34. 7Zr15 shape memory alloy," *Materials Science and Engineering: A,* vol. 655, pp. 193-203, 2016.

[96] D. Golberg *et al.*, "Characteristics of Ti50Pd30Ni20 high-temperature shape memory alloy," *Intermetallics,* vol. 3, no. 1, pp. 35-46, 1995.

[97] C. Grossmann, J. Frenzel, V. Sampath, T. Depka, and G. Eggeler, "Elementary transformation and deformation processes and the cyclic stability of NiTi and NiTiCu shape memory spring actuators," *Metallurgical and Materials Transactions A,* vol. 40, no. 11, pp. 2530-2544, 2009.

[98] C. Grossmann *et al.*, "Processing and property assessment of NiTi and NiTiCu shape memory actuator springs," *Materialwissenschaft Und Werkstofftechnik:*

Entwicklung, Fertigung, Prüfung, Eigenschaften Und Anwendungen Technischer Werkstoffe, vol. 39, no. 8, pp. 499-510, 2008.

[99] H. Karaca *et al.*, "Effects of nanoprecipitation on the shape memory and material properties of an Ni-rich NiTiHf high temperature shape memory alloy," *Acta Materialia*, vol. 61, no. 19, pp. 7422-7431, 2013.

[100] M. I. Khan, H. Y. Kim, Y. Namigata, T.-h. Nam, and S. Miyazaki, "Combined effects of work hardening and precipitation strengthening on the cyclic stability of TiNiPdCu-based high-temperature shape memory alloys," *Acta materialia*, vol. 61, no. 13, pp. 4797-4810, 2013.

[101] M. I. Khan, H. Y. Kim, T.-h. Nam, and S. Miyazaki, "Formation of nanoscaled precipitates and their effects on the high-temperature shape-memory characteristics of a Ti50Ni15Pd25Cu10 alloy," *Acta materialia*, vol. 60, no. 16, pp. 5900-5913, 2012.

[102] K. M. Kim, J. K. Hong, C. H. Park, and J.-T. Yeom, "Comparative Study of the Thermocyclic Behavior of Ti–Ni–Hf and Ti–Ni–Hf–Ta Shape Memory Alloys," *Journal of Nanoscience and Nanotechnology*, vol. 16, no. 11, pp. 11775-11778, 2016.

[103] B. Lin, K. Gall, H. J. Maier, and R. Waldron, "Structure and thermomechanical behavior of NiTiPt shape memory alloy wires," *Acta biomaterialia*, vol. 5, no. 1, pp. 257-267, 2009.

[104] M. Moshref-Javadi, S. H. Seyedein, M. T. Salehi, and M. R. Aboutalebi, "Age-induced multi-stage transformation in a Ni-rich NiTiHf alloy," *Acta materialia*, vol. 61, no. 7, pp. 2583-2594, 2013.

[105] L. Rong, D. A. Miller, and D. C. Lagoudas, "Transformation behavior in a thermomechanically cycled TiNiCu alloy," *Metallurgical and materials transactions A*, vol. 32, no. 11, pp. 2689-2693, 2001.

[106] S. M. Saghaian, *Shape memory behavior of single crystal and polycrystalline Ni-rich NiTiHf high temperature shape memory alloys*. University of Kentucky, 2015.

[107] S. Shimizu, Y. Xu, E. Okunishi, S. Tanaka, K. Otsuka, and K. Mitose, "Improvement of shape memory characteristics by precipitation-hardening of Ti□ Pd□ Ni alloys," *Materials letters*, vol. 34, no. 1-2, pp. 23-29, 1998.

[108] Y. Shugo, T. Shimizu, K. Morii, T. Yamada, and K. Kusaka, "Effects of heat treatment and thermal cycle on helical spring properties in NiTiCu alloy," in *Proceed. of the International Conference on Martensitic Trnaformation, Monterrey*, 1993, p. 1259.

[109] S. Tan, S. Miyazaki, T. Ueki, and H. Horikawa, "Ti-content and annealing temperature dependence of transformation behavior of TiXNi (92-XCu8 shape memory alloys," *Materials Science and Engineering: A*, vol. 230, no. 1-2, pp. 132-138, 1997.

[110] Q. Tian and J. Wu, "Dynamic properties of Ti51Pd30Ni19 high-temperature shape memory alloy under different heat treatment conditions," *Scandinavian journal of metallurgy*, vol. 31, no. 4, pp. 251-255, 2002.

[111] C. C. Wojcik, "Properties and heat treatment of high transition temperature Ni-Ti-Hf alloys," *Journal of materials engineering and performance*, vol. 18, no. 5, pp. 511-516, 2009.

[112] X. Yi, W. Gao, X. Meng, Z. Gao, W. Cai, and L. Zhao, "Martensitic transformation behaviors and mechanical properties of (Ti36Ni49Hf15) 100-xYx high temperature shape memory alloys," *Journal of Alloys and Compounds*, vol. 705, pp. 98-104, 2017.

[113] T. H. Nam, T. Saburi, Y. Nakata, and K. i. Shimizu, "Shape memory characteristics and lattice deformation in Ti–Ni–Cu alloys," *Materials Transactions, JIM*, vol. 31, no. 12, pp. 1050-1056, 1990.

[114] W. J. Zhu, L. I. Duarte, and C. Leinenbach, "Experimental study and thermodynamic assessment of the Cu–Ni–Ti system," *Calphad*, vol. 47, pp. 9-22, 2014/12/01/ 2014, doi: https://doi.org/10.1016/j.calphad.2014.06.002.

[115] X.-m. He, L.-z. Zhao, X.-m. Wang, R.-f. Zhang, and M.-s. Li, "Transformation behaviour with thermal cycling in Ti50Ni43Cu7 shape memory alloy," *Materials Science and Engineering: A*, vol. 427, no. 1-2, pp. 327-330, 2006.

[116] T. Nam, G. Ha, H. Lee, and S. Hur, "Effect of thermal cycling on martensitic transformation temperatures in Ti–Ni–Cu shape memory alloys," *Materials science and technology*, vol. 16, no. 9, pp. 1017-1021, 2000.

[117] R.-D. Jean and J.-B. Duh, "The thermal cycling effect on Ti-Ni-Cu shape memory alloy," *Scripta metallurgica et materialia,* vol. 32, no. 6, 1995.

[118] R. Zarnetta *et al.*, "Identification of quaternary shape memory alloys with near-zero thermal hysteresis and unprecedented functional stability," *Advanced Functional Materials,* vol. 20, no. 12, pp. 1917-1923, 2010.

[119] E. Acar, S. Saedi, G. P. Toker, H. Tobe, and H. E. Karaca, "Post-aging cooling rate effects in Ni45.3Ti34.7Hf15Pd5 shape memory alloys," *Materials Research Bulletin,* vol. 133, p. 111016, 2021/01/01/ 2021, doi: https://doi.org/10.1016/j.materresbull.2020.111016.

[120] C. A. Canbay, O. Karaduman, N. Ünlü, S. A. Baiz, and İ. Özkul, "Heat treatment and quenching media effects on the thermodynamical, thermoelastical and structural characteristics of a new Cu-based quaternary shape memory alloy," *Composites Part B: Engineering,* vol. 174, p. 106940, 2019/10/01/ 2019, doi: https://doi.org/10.1016/j.compositesb.2019.106940.

[121] J. Carrete *et al.*, "Phonon transport across crystal-phase interfaces and twin boundaries in semiconducting nanowires," *Nanoscale,* 10.1039/C9NR05274G vol. 11, no. 34, pp. 16007-16016, 2019, doi: 10.1039/C9NR05274G.

[122] *Standard Test Method for Transformation Temperature of Nickel-Titanium Alloys by Thermal Analysis,* ASTM F2004-17, A. International, 2017. [Online]. Available: www.astm.org

[123] N. H. W. Trehern, R. Ortiz-Ayala, D.J. Sharar, A.A. Wilson, R. Seede, K.C. Atli, A.C. Leff, I. Karaman, "Identification and Design of NiTiCu Shape Memory

Alloys with Small Overall Transformation Range for Phase Change Material Applications," 2021.

[124] D. E. Hodgson, M. H. Wu, and R. J. Biermann, "Shape Memory Alloys," *vol. 2, Properties and Selection: Nonferrous Alloys and Special-Purpose Materials*, A. S. M. H. Committee, Ed.: ASM International, 1990, p. 0. [Online]. Available: https://doi.org/10.31399/asm.hb.v02.a0001100

[125] Z. Stošić *et al.*, "Effects of Composition and Thermal Treatment of Cu-Al-Zn Alloys with Low Content of Al on their Shape-memory Properties," *Materials Research*, vol. 20, 10/01 2017, doi: 10.1590/1980-5373-mr-2017-0153.

[126] R. Agnihotri and S. Bhardwaj, "Synthesis and characterization of Cuznal based shape memory alloys and to optimize behavior on different properties by varying weight percentage," *International Journal of Materials Science and Engineering*, vol. 4, pp. 229-234, 2016.

[127] M. Chandrasekaran, E. Cesari, J. Wolska, I. Hurtado, R. Stalmans, and J. Dutkiewicz, "Stabilisation of Martensite in Copper Based Shape Memory Alloys," (in English), *Journal de Physique IV Proceedings*, vol. 05, no. C2, pp. C2-143-C2-152, 1995 1995, doi: 10.1051/jp4:1995222.

[128] S. S. Leu and C. T. Hu, "Up-quenching effect on the stabilization process of a CuZnAl martensite," *Materials Science and Engineering A-structural Materials Properties Microstructure and Processing*, vol. 117, pp. 247-254, 1989.

[129] A. Abidali, "Effect of aging and step -quenched heat treatment on the Martensitic transformation of CuZnAl shape memory alloy," 10/18 2019.

[130] A. E-11, "Standard test method for determining specific heat capacity by differential scanning calorimetry," ed, 2011.

[131] V. Asanovic, K. Delijić, and N. Jauković, "A study of transformations of β-phase in Cu–Zn–Al shape memory alloys," *Scripta Materialia - SCRIPTA MATER,* vol. 58, pp. 599-601, 04/01 2008, doi: 10.1016/j.scriptamat.2007.11.033.

[132] A. Planes, R. Romero, and M. Ahlers, "The martensitic transition temperature in ternary Cu-Zn-Al alloys," Argentina, 1990. [Online]. Available: http://inis.iaea.org/search/search.aspx?orig_q=RN:22045973

[133] S. Qian *et al.*, "Elastocaloric effect in CuAlZn and CuAlMn shape memory alloys under compression," (in eng), *Philos Trans A Math Phys Eng Sci,* vol. 374, no. 2074, p. 20150309, 2016, doi: 10.1098/rsta.2015.0309.

[134] Y. Wu, E. Ertekin, and H. Sehitoglu, "Elastocaloric cooling capacity of shape memory alloys – Role of deformation temperatures, mechanical cycling, stress hysteresis and inhomogeneity of transformation," *Acta Materialia,* vol. 135, pp. 158-176, 2017/08/15/ 2017, doi: https://doi.org/10.1016/j.actamat.2017.06.012.

[135] F. Zhang, H. Liu, X. Wang, X. Wang, E. Cui, and L. Wang, "Form-stable paraffin/rice straw/polyvinyl alcohol composite phase change material for thermal energy storage," *Materials Letters,* vol. 294, p. 129790, 2021/07/01/ 2021, doi: https://doi.org/10.1016/j.matlet.2021.129790.

[136] A. Liu, X. Meng, W. Cai, and L. C. Zhao, "Effect of Ce addition on martensitic transformation behavior of TiNi shape memory alloys," in *Materials Science Forum*, 2005, vol. 475: Trans Tech Publ, pp. 1973-1976.

[137] S. Hsieh and S. Wu, "A study on ternary Ti-rich TiNiZr shape memory alloys," *Materials characterization,* vol. 41, no. 4, pp. 151-162, 1998.

[138] I. M. Khan, H. Y. Kim, T.-h. Nam, and S. Miyazaki, "Effect of Cu addition on the high temperature shape memory properties of Ti50Ni25Pd25 alloy," *Journal of Alloys and Compounds,* vol. 577, pp. S383-S387, 2013.

[139] T. T. Sasaki, B. C. Hornbuckle, R. D. Noebe, G. S. Bigelow, M. L. Weaver, and G. B. Thompson, "Effect of aging on microstructure and shape memory properties of a Ni-48Ti-25Pd (At. Pct) alloy," *Metallurgical and Materials Transactions A,* vol. 44, no. 3, pp. 1388-1400, 2013.

[140] K. Ramaiah, C. Saikrishna, and S. Bhaumik, "Ni24. 7Ti50. 3Pd25. 0 high temperature shape memory alloy with narrow thermal hysteresis and high thermal stability," *Materials & Design (1980-2015),* vol. 56, pp. 78-83, 2014.

[141] X. L. Meng, Y. D. Fu, W. Cai, J. Zhang, Q. F. Li, and L. C. Zhao, "Martensitic Transformation Behavior and Shape Memory Effect of an Aged Ni-rich Ti-Ni-Hf High Temperature Shape Memory Alloy," in *Solid State Phenomena*, 2008, vol. 138: Trans Tech Publ, pp. 399-406.

[142] L. Patriarca and H. Sehitoglu, "High-temperature superelasticity of Ni50. 6Ti24. 4Hf25. 0 shape memory alloy," *Scripta Materialia,* vol. 101, pp. 12-15, 2015.

[143] B. Hornbuckle, T. Sasaki, G. Bigelow, R. Noebe, M. Weaver, and G. Thompson, "Structure–property relationships in a precipitation strengthened Ni–29.7 Ti–20Hf (at%) shape memory alloy," *Materials Science and Engineering: A,* vol. 637, pp. 63-69, 2015.

7. APPENDIX

IDENTIFICATION AND DESIGN OF NITICU SHAPE MEMORY ALLOYS WITH SMALL TRANSFORMATION RANGE FOR PHASE CHANGE MATERIAL APPLICATIONS: SUPPLEMENTARY MATERIALS

In order to further illustrate the effect of composition and processing parameters on overall transformation range (OTR) and peak offset, NiTi, NiTiPd, and NiTiHf adapted differential scanning calorimetry (DSC) plots are shown in Fig. 7.1.

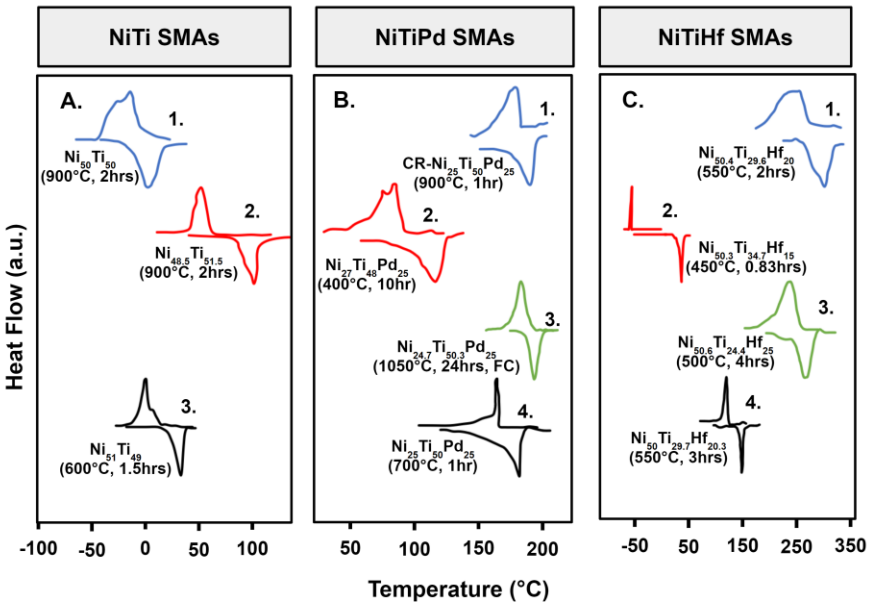

Fig. 7.1. (a) Adapted DSC plots from NiTi literature for solution annealed $Ni_{50}Ti_{50}$ (1 - Liu et al[136]), solution annealed $Ni_{48.5}Ti_{51.5}$ (2 - Hsieh et al[137]), and aged $Ni_{51}Ti_{49}$ (3 - Lin et al[103]). (b) Adapted DSC plots from NiTiPd literature for cold rolled then solution annealed $Ni_{25}Ti_{50}Pd_{25}$ (1 - Khan et al[138]), aged $Ni_{27}Ti_{48}Pd_{25}$ (2 – Sasaki et al[139]),

solution annealed then furnace cooled $Ni_{24.7}Ti_{50.3}Pd_{25}$ (3 – Ramaiah et al[140]), and aged $Ni_{25}Ti_{50}Pd_{25}$ (4 – Khan et al[100]). (c) Adapted DSC plots from NiTiHf literature for aged $Ni_{50.4}Ti_{29.6}Hf_{20}$ (1 – Meng et al[141]), aged $Ni_{50.3}Ti_{34.7}Hf_{15}$ (2 – Evirgen et al[93]), aged $Ni_{50.6}Ti_{24.4}Hf_{25}$ (3 – Patriarca et al[142]), and aged $Ni_{50}Ti_{29.7}Hf_{20.3}$ (4 – Hornbuckle et al[143]).

The compositions of the transforming matrix, second phase - $(Cu, Ni)_2Ti$, and the black particles - $Ti_2(Cu, Ni)$ were confirmed using SEM/EDX. A representative microstructure can be found in Fig. 7.2. The EDX Ti content shows little variation among the three phases of interest (Fig. 7.3(a)). Ni and Cu contents vary with respect to each other, and these variations are shown for the transforming matrix and for the second phase (Fig. 7.3(b)). The transformation temperatures, M_f and A_f, and the transformation range are plotted against the Ni content confirmed by EDX in Fig. 7.3(c) and 7.3(d), respectively.

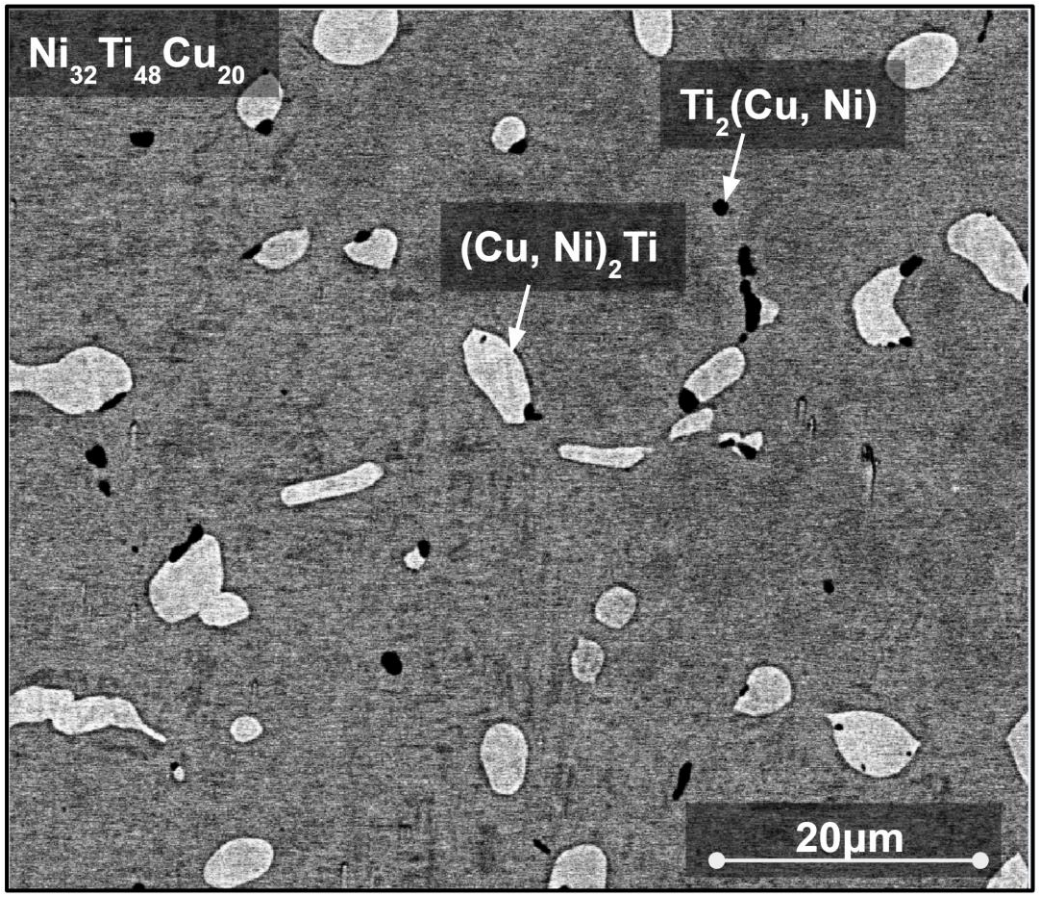

Fig. 7.2. Representative SEM/BSE image of a NiTiCu SMA.

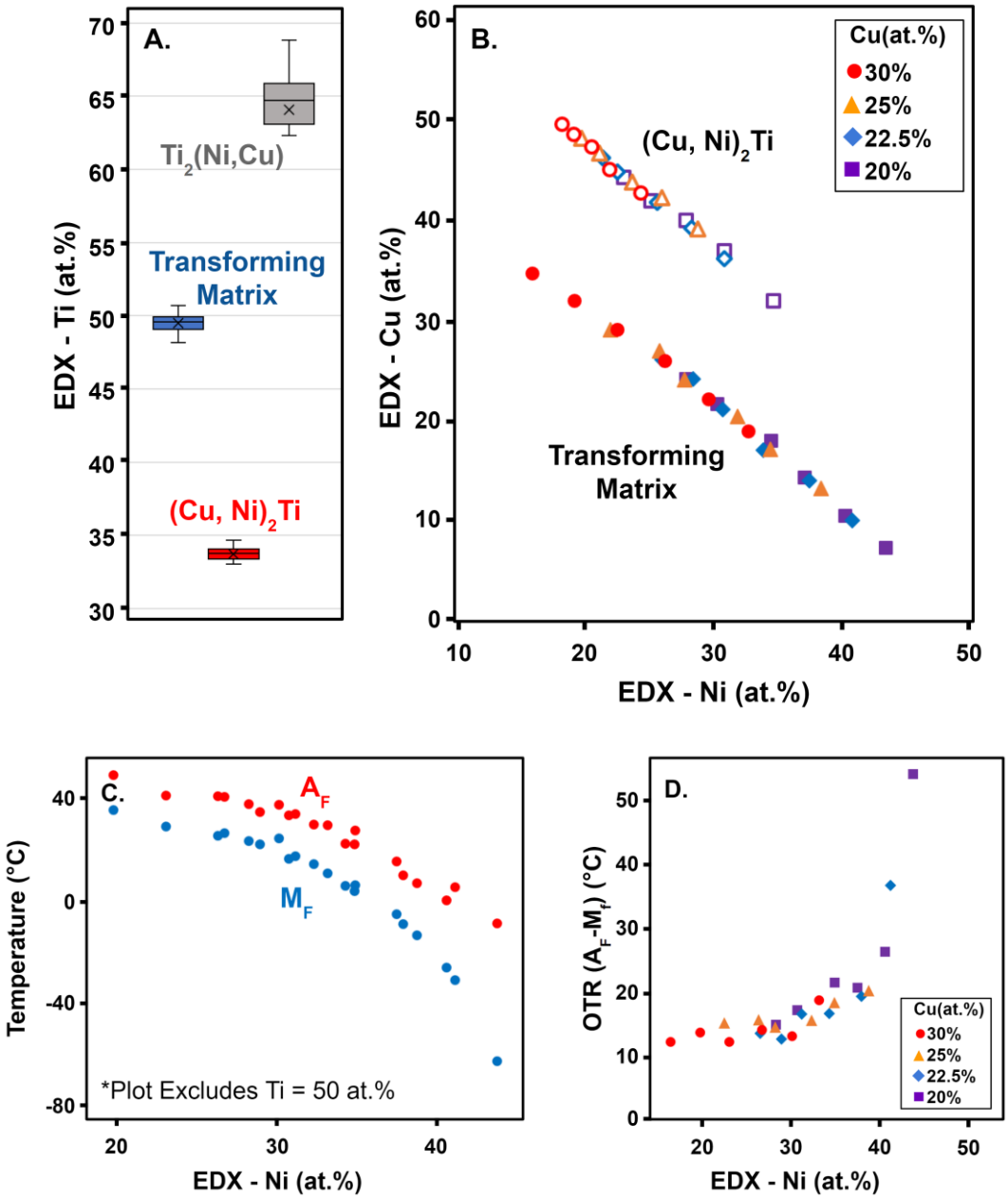

Fig. 7.3 (a) Ti content of the transforming matrix, the second phase, and the black precipitates from SEM/EDX. (b) The Ni and Cu content of the transforming matrix and the second phase from each NiTiCu composition. (c) The A_f and M_f temperatures versus confirmed Ni content, excluding Ti = 50 at.%. (d) The transformation range versus confirmed Ni content for all NiTiCu compositions.

The latent heat of transformation can be normalized by the mass fraction of the transforming phase in order to determine the true transformation enthalpy of the transforming phase. Using the trends in measured density for the alloys from Fig. 3.5(c) in the manuscript, the densities can be approximated for the transforming matrix (ρ_m = 6333 kg/m^3) and for the second phase (ρ_{sp} = 7611 kg/m^3). Next, using the area fraction of the second phase (A_{sp}), the mass fraction of the transforming matrix, M_m, can be approximated by Eq. 5.1:

$$M_m = 1 - \frac{(A_{sp} \cdot \rho_{sp})}{(A_{sp} \cdot \rho_{sp}) + ((1 - A_{sp}) \cdot \rho_m)} \qquad \text{Eq. 5.1}$$

The calculated M_m is then used to normalize the latent heat of transformation by Eq. 5.2

$$\Delta H_{norm} = \frac{\Delta H_{M-A}}{M_m} \qquad \text{Eq. 5.2}$$

The normalized latent heat versus second phase area fraction is shown in Fig. 7.4(a). The results indicate that some other mechanism besides the changing volume fraction of transforming material affects the transformation enthalpy, as the normalized latent heat is still dependent on the amount of second phase. It is possible that different martensitic variants could be decreased in different amounts by the second phase, nanoparticles could be present in the transforming phase, or some other second phase formation related effect could be occurring. The effect of Ni content (as confirmed by EDX) on enthalpy was also explored (Fig. 7.4(b)) revealing decreasing trends with Ni content for various nominal Cu contents, but the separation between the different nominal Cu contents suggests the variation in enthalpy is independent of composition.

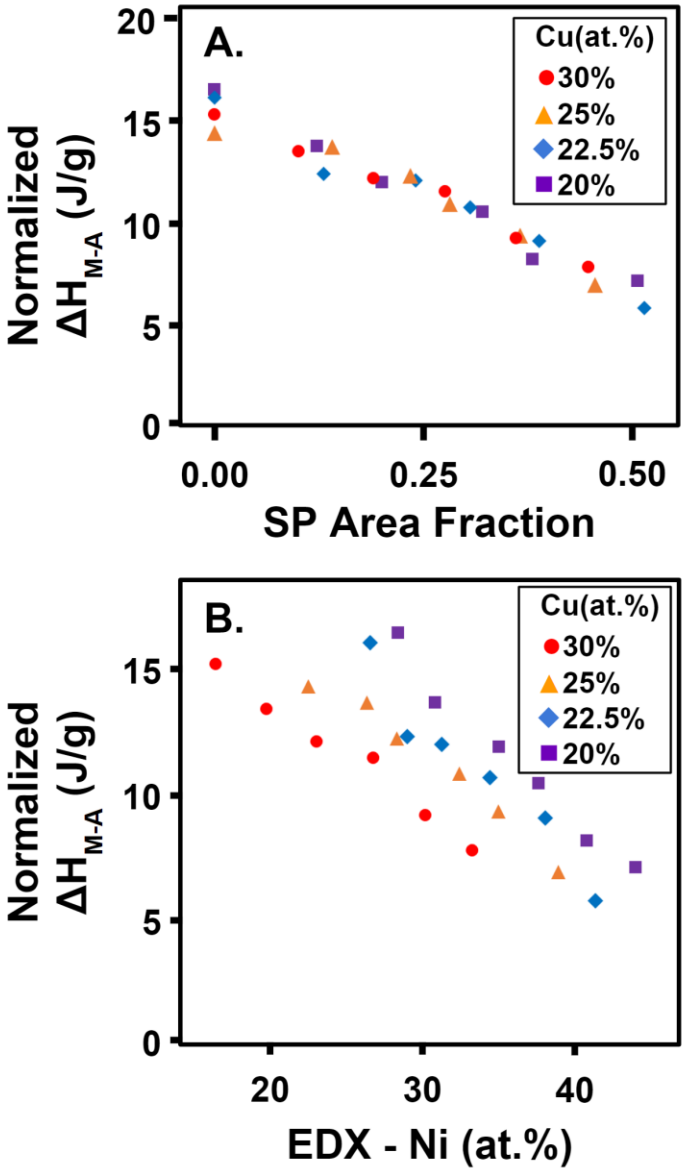

Fig. 7.4 (a) The normalized latent heat of transformation versus second phase area fraction. (b) The normalized latent heat of transformation versus confirmed Ni content. These figures indicate the cause of the decrease in latent heat is not fully explained by the normalizing of the latent heat by the transforming mass.